

Article

A Numerical Investigation to Calculate Ultimate Limit State Capacity of Cable Bolts Subjected to Impact Loading

Faham Tahmasebinia ^{1,*}, Adam Yang ¹, Patrick Feghali ¹ and Krzysztof Skrzypkowski ^{2,*}¹ School of Civil Engineering, The University of Sydney, Darlingtown, NSW 2006, Australia² Faculty of Civil Engineering and Resource Management, AGH University of Science and Technology, Mickiewicza 30 Av., 30-059 Krakow, Poland

* Correspondence: faham.tahmasebinia@sydney.edu.au (F.T.); skrzytko@agh.edu.pl (K.S.)

Abstract: As rock bursts are unavoidable in deep mines and excavations with high in-situ stresses, ground support systems are implemented to manage and mitigate rock bursts. Cable bolts are commonly used as reinforcing elements in ground support systems, which are subject to dynamic loads in burst-prone excavations. To design an efficient cable bolt in burst-prone conditions, shear and energy absorption capacity must be considered. Numerical modelling is an advantageous method of repeatable testing and it is inexpensive and non-destructive. This study develops a statically and dynamically loaded numerical model of a double shear test in ABAQUS/Explicit. A total of 36 static and 576 dynamic tests are carried out, which examine the influence of bolt diameter, steel yield and ultimate strength, dynamic load velocity and dynamic load mass on the displacement, shear force and energy absorption capacity of cable bolts. As bolt diameter and steel yield strength increases, the maximum shear force resisted and bolt displacement increases. Similarly, as the mass and velocity of the dynamic load increases, the amount of energy absorbed by the cable bolt increases. The main novelty of the current research is to suggest a reliable computational tool to investigate the influence of the different key parameters in the cable bolts on the ultimate capacity. The suggested method is a significantly cost-effective technique compared with the experimental investigations.

Keywords: cable bolt; dynamic loading; double shear test; rock burst; finite element analysis; finite element modelling; ABAQUS; energy absorption



Citation: Tahmasebinia, F.; Yang, A.; Feghali, P.; Skrzypkowski, K. A Numerical Investigation to Calculate Ultimate Limit State Capacity of Cable Bolts Subjected to Impact Loading. *Appl. Sci.* **2023**, *13*, 15. <https://doi.org/10.3390/app13010015>

Academic Editor: Arcady Dyskin

Received: 17 November 2022

Revised: 12 December 2022

Accepted: 16 December 2022

Published: 20 December 2022



Copyright: © 2022 by the authors. Licensee MDPI, Basel, Switzerland. This article is an open access article distributed under the terms and conditions of the Creative Commons Attribution (CC BY) license (<https://creativecommons.org/licenses/by/4.0/>).

1. Introduction

With the rising demand for mineral resources sourced through mining and the expansion of geotechnical engineering projects, such as tunnels and other underground structures, mining depth is increasing globally [1]. As depth increases, the greater the in-situ stresses become, furthering the inevitability of seismic events and accompanying rock bursts. Rock bursts cause violent ejections of rock masses and excavation issues due to dynamic rock failure. To counteract their unpredictable behaviour, ground support systems, which comprise of reinforcement and surface support elements are used in excavations. A lack of understanding of dynamic capacity in ground support systems is present and thus this study aims to improve the understanding of cable bolt behaviour under dynamic loading conditions. This will be achieved by carrying out a parametric study using finite element analysis, as it allows for repeated non-destructive testing at a low expense.

This study contains a literature review that investigates existing testing mechanisms with a primary focus on drop testing, blasting and numerical modelling techniques currently used to examine rock burst management, with a focus on ground support systems. This includes a further analysis of rock burst damage mechanisms to understand loading conditions, existing reinforcement and surface elements, current experimental test limitations and the validity of numerical models as a means of testing. A double shear test is numerically modelled in ABAQUS/Explicit to test various cable bolt parameters. The

development of the model is presented, which includes a detailed explanation of all design considerations. The model is calibrated and validated against existing experimental data, and various cable bolt parameters are tested under static and dynamic loading conditions. The results are discussed, and conclusions are drawn consistent with the existing literature. Finally, the limitations of the model are discussed, and further improvements for future work are provided.

2. Literature Review

Rock bursts are dynamic and unpredictable. Because of the unpredictability of rock masses, modelling the theoretical hypocentre of the seismic activity is difficult. Potvin and Wesseloo (2013) [2] have identified five critical factors that contribute to rock burst damage: magnitude of the seismic event, proximity to excavation, localised ground conditions, stress field around the excavation and ground support system design. This is supported by the findings of Durrheim, Milev, Spottiswoode and Vakalisa [3], suggesting that seismic damage is comprised of three main factors, seismic source mechanism, rockburst damage mechanism and the site response. Whilst current modelling methods have not been able to accurately reflect the geological and seismic conditions, testing of ground support system designs can be significantly improved. The following sections will analyse current testing methods and identify trends, conclusions, and inconsistencies of testing.

2.1. Drop Testing

Ground reinforcement and support systems have been a major engineering challenge that has threatened the mining industry due to a lack of adequate testing that has yielded reliable and valid results [4]. Potvin and Wesseloo [2] criticise the lack of further research that has been conducted to meet these design challenges and implores more rigorous testing methods to develop a more comprehensive understanding of dynamic loading induced by seismic activity.

One of the common testing methods is the drop test. It involves directly dropping a large mass onto a reinforcement support element, such as a plate or cable bolt embedded into concrete. An analysis is conducted through a computerised measurement of the forces that are imparted as well as an assessment of the strain and deformations. Tahmasebinia et al. [5] utilised the drop test to measure the non-linear interaction between tensile and shear capacity of cable bolts subject to dynamic loading conditions. It was noted that a key limitation of the test is the consideration of energy loss transfers, such as dissipated losses and shaking of the loaded frame. Additionally, Hadjigeorgiou and Potvin [6] in their assessment of dynamic rock reinforcement and support testing facilities, utilised dynamic testing techniques in the form of drop tests to quantify the performance of ground support systems. Tahmasebinia et al., Hadjigeorgiou and Potvin [5,6] both concluded that whilst the results from the drop test yielded reliable results, these were limited because of the inability to model in-situ conditions and that further testing should be conducted in a capacity that could achieve this. Due to the nature of drop testing, which imparts a singular direct heavy blow, in-situ rock conditions, such as rock mass, stress and boundary conditions are not considered [2,6–8].

Stacey, Potvin and Wesseloo [2,8] highlighted that a critical limitation of the drop test is the physical size restriction of the testing facility. Despite the Western Australia School of Mines (WASM) developing a dynamic testing rig which overcomes this restriction, the dynamic facility does not use a free moving mass impacting a stationary element but instead uses a moving test body, which impacts an energy distribution device or stationary body. In Hadjigeorgiou [6] and Potvin's [6] analysis of the effectiveness of drop tests, they compared several facilities, such as:

- Terratek;
- SRK Drop Weight Test Facility;
- SIMRAC Dynamic Stop Test Facility;
- SRK/Duraset Wedge-Block Loading Device;

- GRC Weight Drop Test;
- Noranda Technology Centre/CANMET Dynamic Testing Apparatus;
- WASM Dynamic Testing Facility;
- MIRARCO Impact Test.

They note that these testing facilities are considered quite poor as they mostly rely on direct impact testing and therefore do not reflect in-situ rock conditions. Whilst they provide a good indication of the support strength of the element itself, they do not adequately simulate the behaviour of support systems under dynamic loading. A benefit of the drop test is that they are generally repeatable and can provide consistent results.

The WASM testing facility is significantly larger and capable of imparting a more significant load and is considered to be the most advanced drop testing facility, however, it cannot overcome the inability to replicate in-situ rock conditions. This is a fundamental flaw of the nature of drop tests. Despite the limitations of the drop test, this testing method is still widely used. Similar to He, Ren and Liu [9], Roberts, Talu and Wang [10] also utilised a static test facility to test varying steel types and examined various connection types noting that it yielded beneficial results. Whilst many have attempted to use the drop test to measure the capabilities of structural elements, it is widely recognised that in terms of measuring the behaviour of elements under dynamic loading that the drop test is not an ideal testing method. Table 1 below summarises the main advantages and disadvantages of drop testing [8].

Table 1. Advantages and disadvantages of drop testing.

Advantages	Disadvantages
Simple and quick to perform	Impact loading may not be representative of rockburst loading
Repeatable results	When impact via a load spreader is used, the true load impacted to the support is unknown
Suitable for comparative testing and quality control testing	Appropriate representation of lateral continuity of support is unlikely to be achieved The effect of the stress in, or confinement or, the rock mass is usually not considered

The WASM facility has been rated as “the most advanced and the closest replication of a seismic event” by Brown [11], the facility successfully measures full scale systems and replicates dynamic loading caused by the ejected rock mass. On top of being able to perform traditional drop testing, the facility has integrated blasting techniques in the form of ejecting rock masses to recreate rock burst effects. Despite the WASM facility being the most advanced testing facility, it still fails to create a simulation that can accurately model the behaviour of rock bursts under various geological strata conditions. Ultimately, there are two primary limitations that drop testing has not successfully overcome, replicating in-situ rock conditions (boundary conditions, rock faults, rock type) and testing a full-scale support system.

2.2. Blasting

The blasting technique utilises an explosive device situated in a borehole near the mine to simulate dynamic loading from seismic activities [12,13]. In contrast to the drop test, this technique considers in-situ rockmass conditions as it is conducted on site [4,7,8]. This was one of the major limitations of drop testing. The blasting experiment involves drilling adjacent bore holes in the walls of the tunnel, filling them with explosives and remotely detonating the load. A high-speed camera is set up inside the excavation to capture the deformation and behaviour of the reinforcement. Mapping of the test site before and after each blast enables a comparison of blasting effects to be monitored. Heal, Hudyma and Potvin [14] utilised Sirovision, a 3D photogrammetry system developed by the CSIRO to map the conditions of the test site. However, it was found that limitations of using this

video-based analysis included potential inaccurate surveying due to movement of control points after blasting which can cause errors in measurement of angles and distances on the digital images.

In the Heal et al. [14], assessment of in-situ performance of ground support systems subjected to dynamic loading, blasting was the primary technique chosen. Their goal was to investigate rockmass discontinuities, rockmass damage, stress conditions on rockburst damage and the influence of support and reinforcement systems. A diagram of their set up can be seen below in Figure 1.

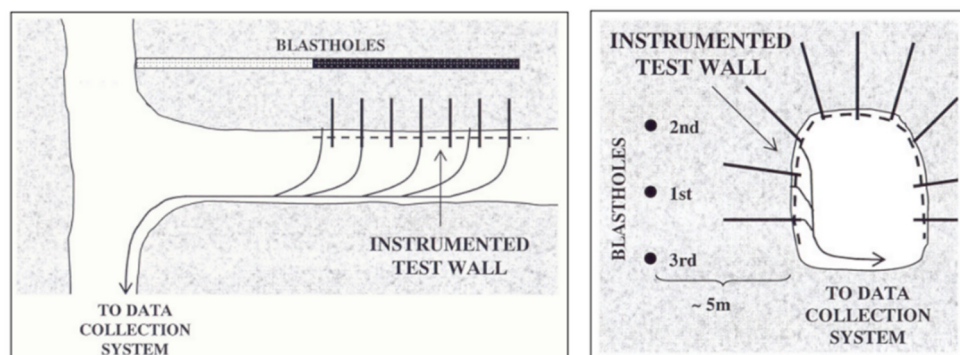


Figure 1. Concept diagram of blasting.

To measure the progressive influence of an increased dynamic load on the wall, each blasthole was separately charged and detonated. A benefit of testing at several borehole locations is that it allows the obtainment of data on various locations of the same excavation. Hildyard and Milev [12] stated that there are 6 elements of control, charge-length, borehole diameter, velocity of detonation, pressure function, rise-time, and peak pressure. Additionally, Heal et al. [14] highlighted that another fundamental flaw was the utilisation of gas-powered explosives, such as ANFO as they generate rapidly expanding blast gasses. This could potentially compromise the validity of the results. Emulsion products are favourable, however, due to limitation of products available on site and in the respective country and market, this cannot always be used [14].

Hagan et al. [15] conducted a similar test, utilising MINSIM modelling as opposed to Sirovision. Both tests followed the same methodologies. Hagan et al. had concluded that due to their 5 m blast hole from the tunnel wall, the impacts of rapidly expanding gas effects would be minimised. These tests could have been improved by utilising an emulsion-based explosive which would eliminate these effects. Interestingly, Hagan et al. [15] found that the peak particle velocity (PPV) ranged from 0.7 m/s to 2.5 m/s in low intensity areas whilst high intensity areas experienced speeds up to 3.3 m/s. However, Stacey [8] findings described an average PPV of 10 m/s and in some extreme cases up to 50 m/s. Because dynamic loading capacity is related to ejection velocity of rock particles [7,16], Hagan et al. [15] could have improved their tests by increasing the charge load to induce rock ejection velocities similar to that documented by Stacey (2012). Archibald, Baidoes, and Katsabanis (2003) experienced similar results in their rock blasting experiment, surprisingly noting that there was minimal damage. This could have been attributed to testing of a single blasthole. To accurately reflect seismic activity through blasting, a stronger explosive strength is required to replicate in-situ dynamic loading.

Whilst blasting has overcome the issue of failing to replicate in-situ rockmass conditions associated with drop testing, this technique is not without its flaws. Blasting involves the use of high-powered explosive devices that are remotely triggered to simulate seismic activity. Upon detonation, underestimation of the damage to the test wall can lead to a complete destruction of the excavation and void the experiment. Additionally, blasting misfires can damage the borehole requiring it to be abandoned due to a tainted rockmass sample. High-speed cameras installed inside the tunnel are subject to shaking and dust,

negatively affecting the accuracy of the digital recording. Camera location is also inhibited due to the spatial orientation of the excavation and suitability of the locations on which the camera can sit.

Blasting is considered an advanced testing mechanism that simulates dynamic loading through the introduction of explosives in tunnels to replicate seismic activity. Whilst this overcomes the key flaw of drop testing, the ability to conduct multiple experiments is limited due to cost and the environment [8]. Compared to drop testing and numerical modelling, the cost of blasting is significantly greater due to equipment and operational costs. As blasting tests are conducted in-situ, to avoid excavation costs, these tests must be carried out in existing abandoned mines. Because of this, it is difficult to repeatedly conduct this type of testing and so the sample size of data is significantly less than other forms of testing. It is ideal to conduct these tests at full magnitude, however, due to a lack of knowledge for support system capabilities and dynamic loading understanding, performing these tests at full scale is not feasible [8,17]. The safety concerns along with the lack of knowledge prevents testing to be conducted at significant magnitudes, ultimately, preventing blast testing to achieve peak effectiveness.

2.3. Numerical Analysis

With the large technological growth and capabilities of computers, the shift to utilising technological innovations to conduct analyses has become more prevalent. It is only natural that numerical modelling has become the next progressive step for scholars to model the reactionary behaviour of rockbursts.

Numerical modelling was first introduced in the 1960s [18], however, it was not till the 1970s that this was applied to the analysis of rockbursts. The first notable use of numerical modelling was conducted by Miranda (1972) [19]. The results from the simulation of the elastic pulse propagation problem of the Split-Hopkinson Pressure bar agreed with the derived strain and strain–time curves. This was the first time numerical modelling was recognised as a potential new analytical model. Blake (1972), had used the FEM to study pillar bursts. From his analysis, he concluded that areas of high stress concentrations are strong predictors of rockburst locations, now a commonly supported theory [7–22]. Jing and Hudson (2002) [18,23] classified numerical approaches as continuum, discontinuum and hybrid methods, a summary of their findings can be seen below in Table 2.

The application of numerical analysis has spanned across many areas of rock mechanics and has proven to yield reliable results, particularly concerning tunnelling and deep mining excavation [24–26]. Whilst numerical modelling generally shows strong positive results that agree with analytical equations, it is not without its flaws. FDM code STEALTH and the BEM Code, MINAP was used to evaluate rock failure and dynamic instabilities. In the study, it was remarked that the stored energy results obtained from MINAP, which used the elastic constitutive model, was smaller than STEALTH which employed a non-constitutive model. Wang et al. (2021) highlights the importance of careful selection of various numerical modelling software suggesting that there needs to be compatibility between the fundamental principles of the software, the rockburst mechanism and the specific engineering situation.

Wang et al. (2021) [27], highlights the capabilities of numerical modelling to be an accurate form of analysis to examine various loading and encourages the use of numerical modelling as technological capabilities and skills grow. However, concern for the ability to accurately model boundary conditions has been the primary issue and limitation of numerical modelling [25–28].

Numerical modelling has grown to become a primary form of analysis. It has seen a growth in usage amongst researchers as a complimentary method of supporting field testing. Hildyard and Milev (2001) [12], utilised both blasting and numerical modelling to model wave propagation due to seismic activity. They concluded that the numerical waveform corresponded closely to the analytical result which was supported by their collaborative blast model indicating realistic tunnel motions that were to be replicated through their

numerical model. Similarly, in the Tahmasebinia, Zhang, Canbulat, Vardar, and Saydam (2018) study, they investigated the development of a numerical model to test the structural response of cable bolts subject to static and dynamic loading, with a particular focus on shearing effects. These results were compared with Mirzaghobanali et al. (2017) [29] double shear testing which agreed with the results obtained from the ABAQUS model. As further research continues to investigate combined support systems subject to dynamic loading through the use of numerical analysis, testing can be replicated in a safe, repeatable and cost-friendly manner [6,30]. (Krykovskiy, Krykovska, & Skipochka, 2021) [30–38] also presented a significant contribution to the latest research in the current field.

Table 2. Summary of numerical analysis classifications.

Numerical Approach	Subtype	Commercial/Academic Code	Institution/Author (Year)
Continuum method	Finite element method (FEM)	ABAQUS	Dassault Systemes
		ADINA	ADINA R&D, Inc.
		ANSYS	ANSYS, Inc
		GEO5	Fine Software
		LS-DYNA	LSTC
		Midas GTS NX	MIDAS IT
		PLAXIS2D, PLAXIS3D	Plaxis
		RFFA2D, RFFA3D	Mechsoft
		RS2 (Phase 2), RS3	Rosceience
		FLAC, FLAC3D	Itasca Consulting Group, Inc.
Discontinuum method	Boundary element method (BEM)	Examine	Rosceience
		Map3D Non-Linear	Map3D
	Discrete element method (DEM)	PFC2D, PFC3D	Itasca Consulting Group, Inc.
		UDEC, 3DEC	Itasca Consulting Group, Inc.
		Discontinuous deformation analysis (DDA)	DDA codes
Hybrid method	Discrete fracture network (DFN)	FracMan	Golder
		NAPSAC	AEA Technology
	BEM/DEM	DEM_SRS + BEDA + FNET	Wei (1992), Wei and Hudson (1998)
		+ BEFA	Zienkiewicz et al. (1977)
		BEM/FEM codes	Fakhimi (2009)
		CA3	Rockfield
		ELFEN	Geomechanica
		IRAZU	Shi (1991)
		NMM	Munjiza et al. (2004)
		Y2D	Mahabadi et al. (2012)
DEM/FDM	PFC2D/FLAC, PFC3D/FLAC3D	Itasca Consulting Group, Inc.	
Y-Geo			

2.4. Summary

The need to conduct further research and testing is paramount in developing a comprehensive understanding of the interaction between seismic activity and rock bursts under combined loading is of the utmost importance. Through current means of analysis and testing, the main barrier of understanding has been the development of a safe, accurate and low-cost option that yields reliable and valid results. Previously, drop testing and blasting was the more common approach, however, there has been a shift to numerical analysis as a viable testing method. With further investigation into the capabilities and utilisation of numerical analysis as a testing method, modelling and analysis can be conducted in a safe, low-cost yet accurate form.

3. Parametric Study of Cable Bolts

Many studies have been conducted on the double shear test using both experimental and numerical analysis, however, there still exists a lack of knowledge of the shear perfor-

mance of yielding bolts in dynamic loading conditions. To conduct a parametric study on the failure mechanisms of cable bolts under dynamic shear loading conditions, a numerical model of a double shear test will be developed using finite element analysis (FEA) in ABAQUS/Explicit. The utilisation of FEA to model a double shear test under dynamic loading conditions is advantageous as it allows multiple non-destructive cheap tests to be run simultaneously. Additionally, as tests are defined by user inputs, it compliments parametric studies and encourages the investigation of multiple parameters.

Tahmasebinia et al. (2018) [28] created a double shear test using finite element modelling and expressed the value of ABAQUS' ability to model many complex interactions and boundary conditions. Mirzaghobanali et al. (2017) [29] also recognised the advantages of using FEM and conducted a similar double shear test. This study will further the model by investigating the impacts of select parameters on dynamically loaded bolts, with a focus on maximum displacement, shear force and energy absorption. The analysis will examine the bolt diameter, the steel strength, the velocity of the dynamic load cell, and the mass of the dynamic load cell.

To create a model that investigates current cable bolts in the mining industry, all bolts will be modelled to replicate Jenmar's bolt properties as they are currently the industry standard in Australia. Jenmar have published the technical data for all their bolts. Table 3. displays the bolt types, diameters and steel properties that were extracted from Jenmar Technical Brochure that will be used in the analysis.

Table 3. Jenmar bolt properties.

Jenmar Bolt Type	Bolt Diameter (mm)	Typical Yield Strength (kN)	Typical Ultimate Tensile Strength (kN)
17.8 Yield Lok Bolt	18	147	196
J-Tech [®] 20 mm Bolt	20	170	200
Yield Lok [®] Bolt 23 mm	23	245	328
J-Tech [®] 25 mm Bolt	25	245	294
63T Sumo Cable Bolt	28	560	630
70T 12 Wire Sumo Cable Bolt	31	640	705

Furthermore, to create a valid parametric study, the numerical model must be calibrated using reliable experimental data. As no experimental data could be obtained from dynamical tests, a static test was first modelled which was then calibrated, followed by the development of the dynamic test. Experimental data for statically tested cable bolts was extracted from the Australian Coal Industry Research Program's (ACARP) Project C27040 and used to calibrate the model. The laboratory experimental data obtained in part one of the study included conducting double shear tests of various bolts, including Jenmar's 63T Sumo Cable Bolt. Therefore, the statically loaded model will be calibrated using the experimental data obtained from ACARP's Project C27040 and the dynamically loaded model will be calibrated against Tahmasebinia et al. (2018) dynamically loaded FEA double shear test.

4. Materials and Methods

4.1. Developing the Model

To develop the FEA model of the double shear test, a base model was first developed and calibrated in ABAQUS/Explicit. This base model was designed for static loading conditions, where once calibrated, modifications were made to create a new dynamically loaded base model. The process used to develop both the static and dynamic models are detailed below.

4.1.1. Geometry of Parts

To create the double shear test model, three geometric parts were created. These included a cube to represent the rock material, a cylinder to represent the cable bolt under investigation and a sphere to act as a loading mechanism for dynamic testing.

The cube was constructed with an edge length of 500 mm and a circular void that was extruded through the centre of the ZY plane of the cube. The extruded circular void had a diameter equal to the respective bolt diameter under investigation. The cube was then manually subdivided 30 mm from both the top and bottom of the cube to allow for the appointment of rigid bodies. Furthermore, the cube was manually partitioned to improve ABAQUS' automatic meshing tool, which is further discussed in the mesh generation section. A completed cube with a 28 mm diameter void is displayed below in Figure 2.

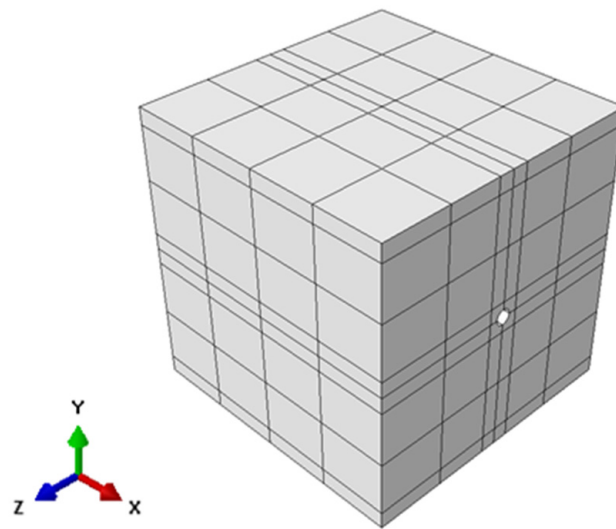


Figure 2. Geometric part—concrete box.

Due to the complex geometric cross-section of dynamic cable bolts, all bolts were modelled as smooth cylinders. Although this reduces the accuracy of the numerical analysis, due to the scope of this study, it is deemed as a justifiable simplification. All bolts were modelled with a length of 1600 mm, with a diameter equal to that of the respective Jennmar bolt being modelled. All bolts were manually partitioned to improve ABAQUS' automatic meshing tool, which is further discussed in the mesh generation section. A completed bolt part is displayed below in Figure 3.



Figure 3. Geometric part—steel bolt.

For dynamic testing, a sphere was created to act as a dynamic load cell. To develop the dynamic model, a sphere with a diameter of 300 mm was created and manually subdivided to improve ABAQUS' automatic meshing tool. A completed sphere part is displayed below in Figure 4.

4.1.2. Material Properties

As a non-linear analysis of cable bolts was conducted, elastic, plastic, shear damage and fracture properties were assigned to the steel bolt. The steel properties tested were extracted from Jennmar's tested data, where the yield and ultimate strength were provided as a force. ABAQUS requires yield and ultimate strength to be inputted as a pressure load, thus yield and ultimate strength were divided by the undeformed cross-sectional

area of the bolt under investigation. The elastic properties of the 63T Sumo Cable Bolt are summarised in Table 4.

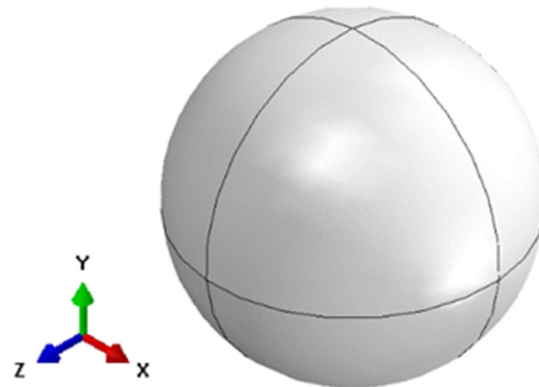


Figure 4. Geometric part—load sphere.

Table 4. Elastic steel properties of the 63T Sumo cable bolt.

Density (kg/m ³)	Elastic Modulus (MPa)	Yield Strength (MPa)	Ultimate Strength (MPa)	Poisson’s Ratio
7800	200,000	922	1031	0.3

To define a smooth transition from elastic to plastic deformation, the Giuffre–Menegotto–Pinto model was used [31].

The plastic behaviour of steel was defined in terms of stress–strain data, which was calculated in accordance with AS4100:2020. To accurately reflect laboratory data, the engineering stress–strain was converted into true stress–strain because engineering stress–strain fails to account for a changing cross-sectional area due to plastic failure. The following equations were used to convert the plastic stress–strain values from engineering to true values [32].

$$\sigma_T = \sigma_E(1 + \epsilon_E) \tag{1}$$

$$\epsilon_T = \ln(1 + \epsilon_E) \tag{2}$$

where σ_T is the true stress, σ_E is the engineering stress, ϵ_T is the true strain and ϵ_E is the engineering strain.

Figure 5 compares the engineering vs. true stress–strain curve of steel with a yield strength of 922 MPa and an ultimate strength of 1031 MPa, that was used to calibrate the static model.

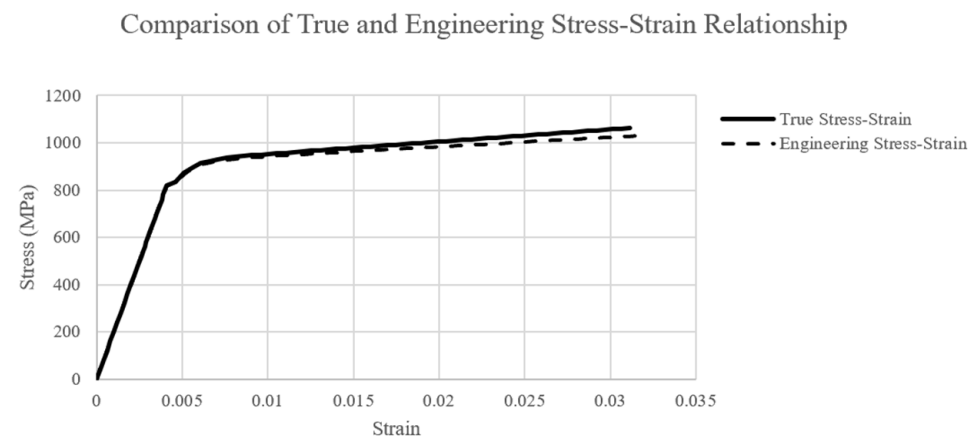


Figure 5. True vs. engineering stress–strain relationship.

The shear damage and fracture properties that were defined for steel with a yield strength of 922 MPa and an ultimate strength of 1031 MPa are summarised below in Table 5.

Table 5. Shear damage and fracture properties of steel.

Fracture Strain	Shear Stress Ratio	Strain Rate	Fracture Energy (N/mm)
0.3	0.13	0.0001	336,302

The fracture energy is defined as the energy required per unit area to change a material surface from its initial unloaded state to a state of complete separation [33]. The fracture energy of a material is estimated by calculating the integral sum of a material's stress–strain curve [34]. To calculate the fracture energy of each tested steel yield and ultimate strength, a Python code was developed, which has been recorded in Appendix A.1.

The concrete box acts as an alternative to rock, where each concrete block represents a layer of rock. This simplification is justified as rock possesses similar properties to concrete, and thus allows for easily repeatable experimental double shear testing. Table 6 summarises the defined concrete material properties for ABAQUS.

Table 6. Material properties of concrete.

Compressive Strength (MPa)	Density (kg/m ³)	Elastic Modulus (MPa)	Poisson's Ratio
40	2400	33,346	0.2

The Drucker–Prager and the Concrete Damage Plasticity (CPD) model were both investigated when calibrating the numerical model. The Drucker–Prager model produced marginally more accurate results to the experimental data. However, the computational time was excessive, thus the CDP model was used. The CDP model defines two primary failure mechanisms, compressive crushing and tensile cracking, which are available in the ABAQUS properties library. The compressive linear elastic range was defined as up to 40% of its compressive strength, and the tensile behaviour was modelled as initially elastic followed by softening after cracking occurred. The damage parameter as a function of inelastic strain were defined in accordance with Sumer and Aktas (2015) [35].

For dynamic testing, the load sphere was also assigned steel properties, however the ball is intended not to deform and hence assigned as a rigid body. Therefore, as the ball does not deform, only elastic material properties were defined. Table 7 summarises the steel load sphere properties inputted into ABAQUS.

Table 7. Steel load cell properties.

Density (kg/m ³)	Elastic Modulus (MPa)	Poisson's Ratio
7800	33346	0.2

4.1.3. Assembly of Parts

The model was assembled such that the bolt was threaded perfectly through the holes of the three concrete boxes. A 50 mm gap was created between each concrete block to prevent the blocks from contacting each other, preventing resistance through friction. This was done such that excess contact properties could be avoided and thus reduce the computational time to run the model. For dynamic tests, the load sphere was placed above the centre of the middle concrete block, where the bottom of the sphere and the top of the central block were in contact. Figure 6 displays the assembled static and dynamic numerical models.

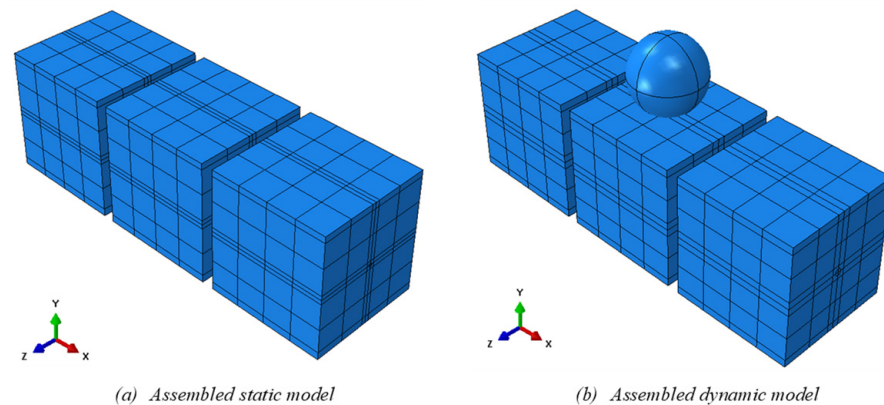


Figure 6. Assembled ABAQUS models (indicated in white).

4.1.4. Rigid Bodies

As the focus of the double shear test and the scope of this study is to conduct a study on bolt performance, rigid bodies will be applied to all concrete boxes to prevent unnecessary deformation. For static testing, the boundary blocks had rigid bodies assigned to the bottom 30 mm partition, whilst the centre block had a rigid body assigned to the top 30 mm partition, which will act as the loading cell. For dynamic testing, all three concrete boxes were assigned a rigid body to the bottom 30 mm partition. As the load sphere deformation is not under investigation, the entire sphere was assigned as a rigid body. Figure 7 displays the assigned rigid bodies in white for both static and dynamic models.

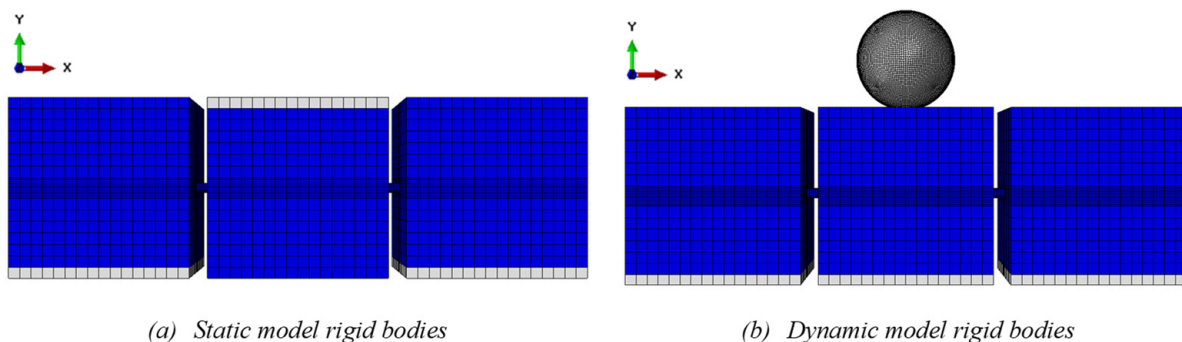


Figure 7. Assigned rigid bodies (indicated in white).

4.1.5. Boundary Conditions and Load Cells

The double shear test requires the two boundary blocks to be fixed in all degrees of freedom, with the centre box restricted to displace in the direction of force applied. To apply this to both the static and dynamic model, the boundary blocks were assigned as rigid bodies and were fixed in all directions and rotational planes. The centre block was fixed in all rotational planes and directions except for the vertical y-plane. For dynamic testing, as shear capacity is the focus of the investigation, the load sphere was fixed in all directions except it was free to move in the vertical plane. To prevent slippage of the bolt during shearing, the ends of the tested bolt were completely fixed.

To apply a load to the numerical test, a boundary condition was applied to the load cell, where the load cell was forced to move downwards in only the vertical direction at a defined velocity. As quasi-static analysis was utilised, the loading rate is negligible if inertial forces do not exceed quasi-static boundaries, thus the load cell (the centre block's rigid body) was forced to move down at a velocity of 100 mm/s. For dynamic testing, the load cell velocity was varied at velocities of 100, 200, 400 and 600 mm/s.

4.1.6. Contact Interactions

Contact properties were defined between the bolt and all three concrete boxes to simulate the interaction between the bolt and rock surface. Surface-to-surface contact properties were assigned to the bolt and the concrete blocks. The concrete block was assigned as the master surface, as it is a rigid body, and the steel bolt was defined as the slave surface. A penalty contact method involving mechanical, tangential and normal properties were assigned to the surface-to-surface contact interactions, as summarised in Table 8. No contact properties were assigned between the concrete blocks, as the 50 mm gap and boundary conditions prevent all contact between concrete blocks.

Table 8. Surface-to-surface contact properties.

Constraint Type	Sliding Formulation	Tangential Behaviour	Normal Behaviour
Penalty Contact	Finite Sliding	Friction Coefficient 0.5	Pressure Overclose Hard Contact

Additionally for the dynamic model, a general surface contact interaction was assigned to the spherical load cell and the top of the central block. In particular, the contact interaction was applied to the bottom half of the sphere, and the entire top face of the central concrete block. In this case, the concrete box was assigned as the slave surface and the load cell was assigned as the master surface. For the general surface contact assignment, a normal behaviour was defined with the default settings available in the ABAQUS/Explicit library, which included default surface thickness, shell/membrane offset, feature edge criteria and surface smoothing settings.

4.1.7. Outputs and Solvers

To record the force and displacement results of each test, a field and history output was assigned to the load cell. Therefore, the recorded values reflect the reaction forces and the displacement of the load cell over a specified test time. The load cells were chosen to measure the output rather than the bolt to reflect how laboratory data is recorded. For static tests, all test time durations were set to 1.5 s such that all tests displayed a peak reaction force. For dynamic tests, all test time durations were set to 0.6 s such that failure of the bolt was captured whilst minimising test and computational time. For static and dynamic results, 200 evenly spaced output data points were specified across the duration of the test

ABAQUS/Explicit and ABAQUS/Standard can be used for static loading conditions, where both solvers solve nodal accelerations and use the same element calculations [36]. ABAQUS/Standard uses an implicit solver, where linear equations are solved using Newton's iterative method, whilst ABAQUS/Explicit solver avoids iterations by explicitly advancing the kinematic state from the preceding iteration. As the model consists of many contact points, convergence issues are likely to occur and thus require more iterations, increasing the computational time significantly when using an implicit solver. Therefore, the model utilised a dynamic explicit solver for both static and dynamic testing.

To utilise a dynamic explicit solver for static testing, a quasi-static analysis is used. This is achieved by accelerating the simulation time such that it is the shortest possible, whilst keeping inertial forces negligible. To ensure inertial forces remain negligible and the loading rate is kept constant, mass-scaling was applied to static tests, as summarised in Table 9.

Table 9. Mass scaling applied to the static test.

Region	Type	Frequency/Interval	Factor	Target Time Increment
Whole Model	Target time Inc.	Beginning of Step	None	1×10^{-5}

4.1.8. Mesh Generation and Calibration

To create a suitable mesh for static and dynamic testing, a brick element is required to create a three-dimensional model. ABAQUS has two standard brick elements, an eight-node linear brick, (C3D8) and an eight-node linear brick with reduced integration and automatic hourglass control (C3D8R). The C3D8 element consists of $2 \times 2 \times 2$ integration points, whilst C3D8R element consists of one central integration point as shown below in Figure 8.

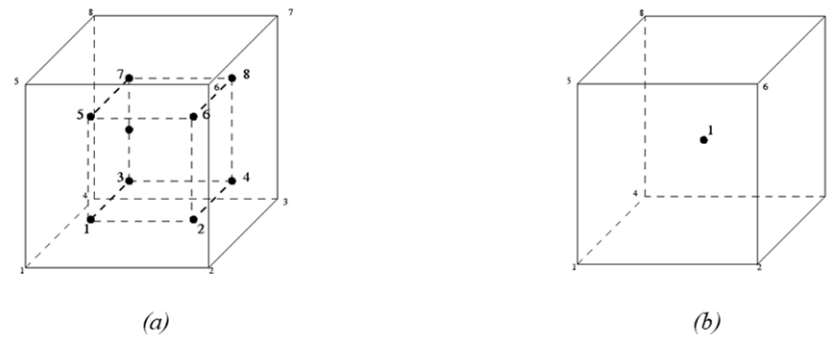


Figure 8. Geometry and integration of brick elements (a) C3D8 and (b) C3D8R.

As the C3D8 element undergoes full integration, the element does not respond well to plastic deformation [36]. Therefore, as the double shear test model investigates plastic deformation of both the bolt under investigation and the concrete encasing, C3D8R elements will be utilised. It should be noted that the integration point is in the centre of the element, thus finer elements are required to display accurate stress concentrations at the boundary of the geometry. The finer a mesh becomes, the greater the computational time, thus a fine mesh will only be utilised in areas of interest.

ABAQUS has an automatic meshing feature which creates a basic mesh when an element seeding size is nominated. To enhance this feature and create a more favourable mesh, manual localised subdivisions are created in individual parts in critical areas including contact regions and areas experiencing large deformation and stress concentrations. Additionally, by creating manual partitions, mesh size in critical areas can be varied without using mesh grading, avoiding irregularly shaped elements. This was applied to the cable bolt and concrete box. The cable bolt shown in Figure 9, demonstrates the effects of manual partitioning prior to auto-meshing compared with no partitions.

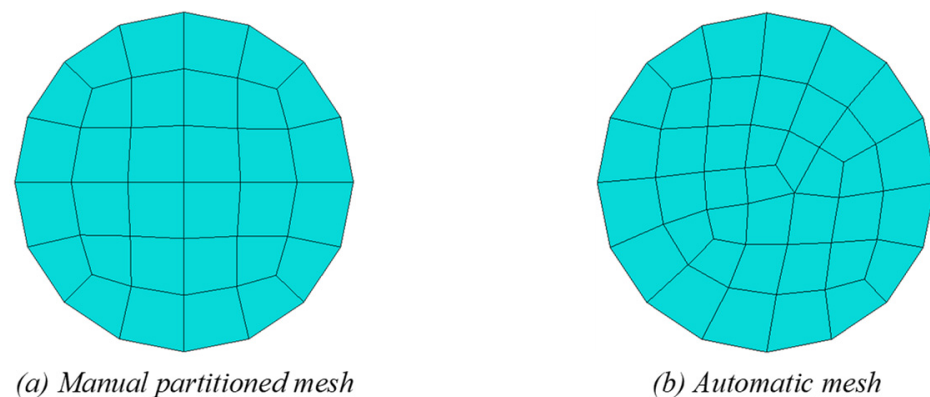


Figure 9. Cross section of steel bolt mesh optimisation.

The mesh size of the concrete surrounding the bolt was fine, while maintaining a coarse mesh in areas of little interest, as demonstrated below in Figure 10.

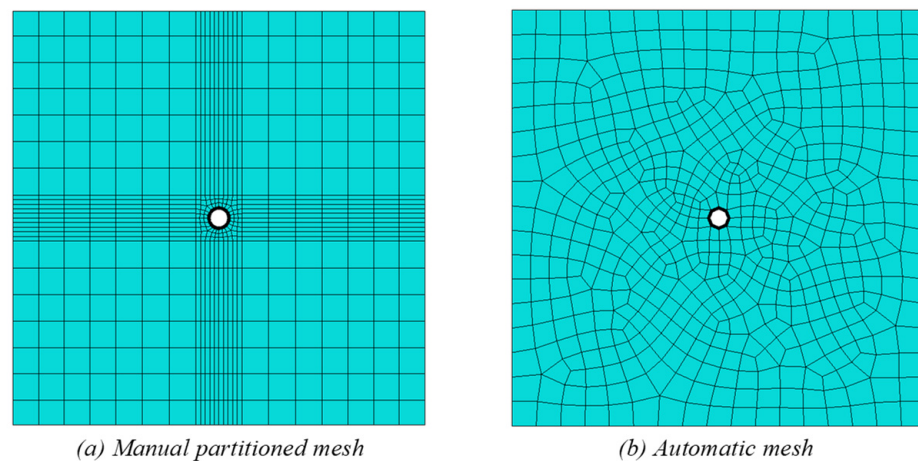


Figure 10. Cross section of concrete box mesh optimization.

As the two boundary blocks of concrete are fixed, the area of interest of the bolt is the region of the bolt encased by the centre block. In addition to the central third of the bolt, the finer mesh was also extended to the 50 mm gaps where the bolt was not encased in concrete. The fine mesh was made twice as fine as the remainder of the bolt, as shown below in Figure 11.



Figure 11. Fine bolt mesh.

To utilise the automatic mesh function, element seeding sizes must be defined in the X, Y and Z planes. Therefore, to mesh the sphere for dynamic tests, manual partitions were created in all three planes such that seeding size could be defined. The meshed sphere is shown below in Figure 12.

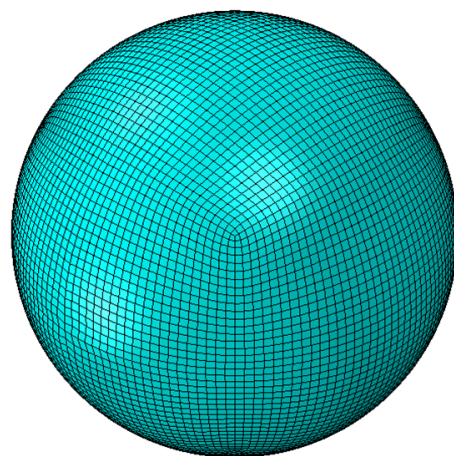


Figure 12. Load sphere mesh.

Once all geometric parts were individually meshed, the assembled static and dynamic model meshes were generated, as shown below in Figure 13.

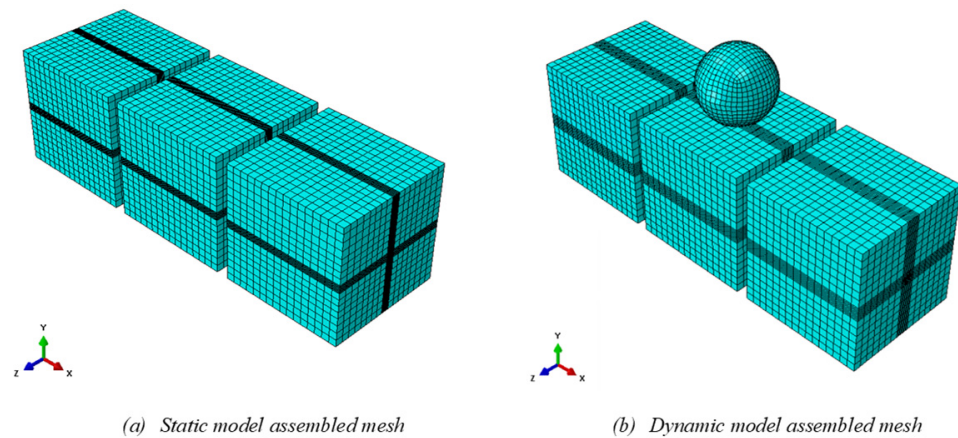


Figure 13. Overall model of mesh.

To determine the exact element seeding size to produce an optimised mesh such that accurate results with minimal computational time were achieved, varying fine mesh sizes were tested against the experimental data, as shown below in Figure 14. A seeding size of 10, 15, 20 and 25% of the bolt’s diameter was tested for the finer central section of the steel bolt where the remainder of the bolt’s mesh was assigned as double the seeding size of the fine mesh. The concrete in contact with the entirety of the bolt was assigned the same seeding size of the bolt’s finest mesh.

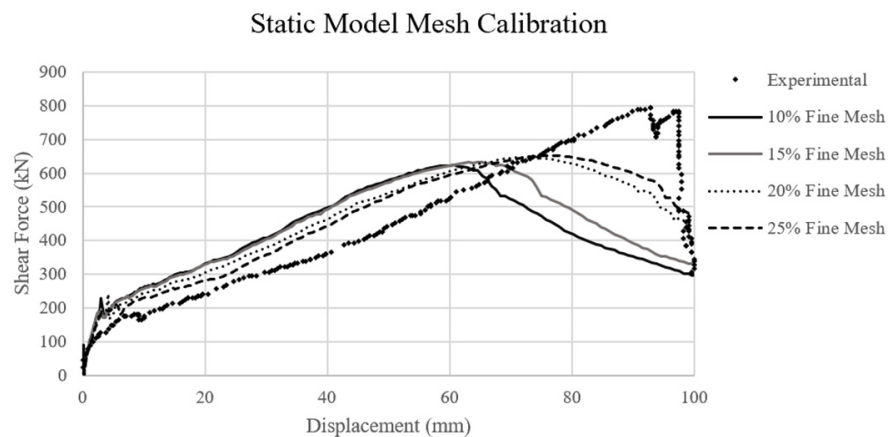


Figure 14. Force vs. displacement graph comparing fine meshes of static model.

Furthermore, the maximum shear force and computational time for each fine mesh has been summarised in Table 10.

Table 10. Computational times of different fine meshes in static testing.

Fine Mesh Seed Size (%)	Maximum Shear Force (kN)	Computational Time (s)
Experimental	795.50	N/A
10	625.77	1746
15	631.81	1025
20	647.92	618
25	652.12	431

All fine meshes that were tested displayed a similar trend to the experimental data within reason. As the mesh became coarser, the computational time decreased significantly, however the maximum shear force became less accurate as the C3D8R elements were utilised. To optimise the accuracy and computational time of the analysis, a fine mesh size of 20% of the bolt diameter under investigation was used for all tests.

To determine an optimal mesh size for the spherical load cell in dynamic testing, a seeding size of 1, 2, 5 and 10% of the sphere’s diameter were tested, as shown in Figure 15. The finer mesh of the concrete box and steel bolt were kept at 20% of the bolt’s diameter.

Dynamic Model Sphere Mesh Comparison

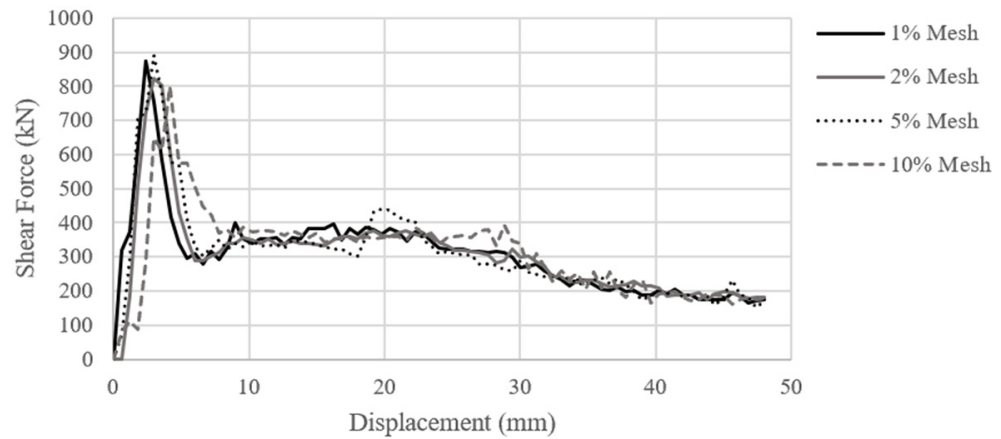


Figure 15. Force vs. displacement graph comparing mesh size of sphere in dynamic testing.

The computational time of each test was recorded in Table 11.

Table 11. Computational times of different fine meshes in dynamic testing.

Fine Mesh Seed Size (%)	Computational Time (s)
1	828
2	341
5	254
10	239

A mesh size of 5 and 10% of the sphere’s diameter had low computational times, however, it displayed excessive fluctuations in the produced force vs. displacement graph above. This indicated greater inaccuracy, thus a finer mesh was required. A mesh seed size of 1% of the sphere’s diameter was too fine, as the computational time was excessive. Hence, a mesh size of 2% of the sphere’s diameter was nominated for dynamic testing. The seeding sizes of all geometric parts of the calibrated model have been summarised in Table 12 below.

Table 12. Calibrated model mesh sizes.

Part	Coarse Mesh Seed Size (mm)	Fine Mesh Seed Size (mm)
Bolt	11.2	5.6
Box	30	5.6
Sphere	N/A	6

4.2. Developing the Model

Prior to performing the parametric analysis, the ABAQUS model was calibrated against experimental data. This was to ensure that the numerical model was replicating experimental data and academic literature. To calibrate the static model, experimental data was utilised from ACARP’s C27040 project, where a double shear test was conducted on a 63T indented Sumo Cable Bolt provided by Jennmar.

The calibration of the numerical model was not expected to be identical to the experimental data due to simplifications made when developing the model. The bolt was created as a smooth cylinder, where the experimental data tested an indented cable bolt. The three

concrete blocks of the laboratory experiment were not the same size, with the centre block being longer than the two boundary blocks. The developed model used three identically sized boxes to minimise the number of geometric parts required. The experimental test also included grouting of the bolt after the concrete blocks were poured, whilst the numerical model excluded grouting and utilised surface-to-surface contact properties to simulate grouting and frictional effects. Furthermore, the laboratory test of the indented 63T Sumo Cable Bolt used was only carried out once, thus the experimental data itself is not reliable. As only one test was conducted per specific bolt, manufacturing defects, instrumental errors and human errors can influence the results.

To calibrate the static numerical model, a comparison of the results of the force vs. displacement of the 63T Sumo Cable Bolt was utilised, as shown below in Figure 16.

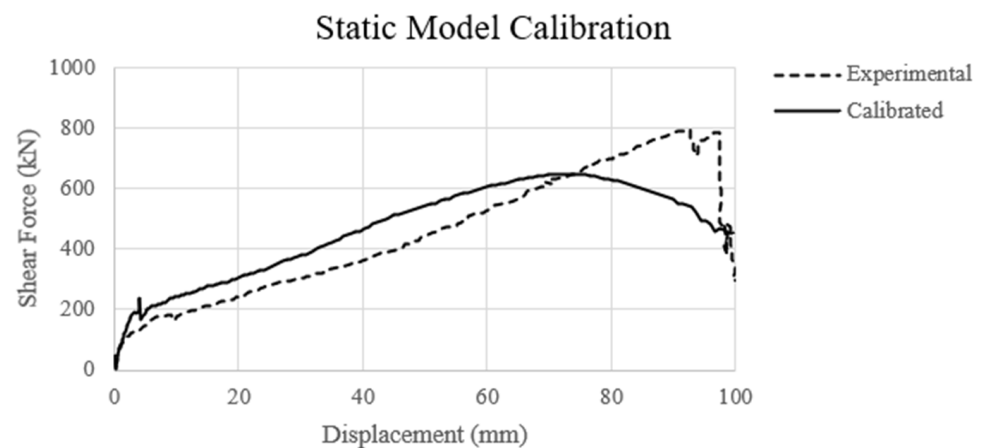


Figure 16. Calibrated vs. experimental force vs. displacement.

The force vs. displacement graph of the calibrated and experimental data shows a similar trend in both the elastic and plastic regions, however, shows differing fracture mechanisms. The experimental data displayed an instantaneous fracture once ultimate shear force was reached, whereas the numerical model displayed a gradual fracture at peak shear force. This was expected due to how the numerical model applies and records shear force. The field and history outputs applied to the model recorded the displacement and reaction forces of the load cell (i.e., top of the concrete block). Once the recorded reaction force of the load begins to decrease, the bolt has fractured and is no longer resisting the applied force. Therefore, from the numerical data, the maximum displacement of the bolt at complete failure occurs at the peak shear force recorded.

To determine the accuracy of the calibration, the peak shear force and its respective displacement will be numerically compared.

$$\frac{\text{Max Shear Force Calibrated}}{\text{Max Shear Force Experimental}} = \frac{647.92 \text{ kN}}{795.50 \text{ kN}} = 81.44 \% \text{ accuracy}$$

$$\frac{\text{Displacement at Failure Calibrated}}{\text{Displacement at Failure Experimental}} = \frac{73.50 \text{ mm}}{92.82 \text{ mm}} = 79.18 \% \text{ accuracy}$$

The numerical model displays an approximate accuracy of 80%, which is deemed reasonable for the simplifications utilised for developing the model. The factors impacting the accuracy of the calibration will be further discussed in the limitations section of this study.

To calibrate the dynamic model, there was no available dynamically loaded double shear test experimental data, thus the calibrated static model was further built upon. Tahmasebinia et al. (2018) [28] modelled a double shear test, thus this model was referenced in the development of the frictionless double shear test model. The load vs. displacement graph for the dynamic model was produced as shown in Figure 17, which shows a similar trend to Tahmasebinia et al. (2018) [28] numerical dynamic impact load vs. displacement results. Thus, for the purpose of this parametric study, the dynamic model was deemed reasonable.

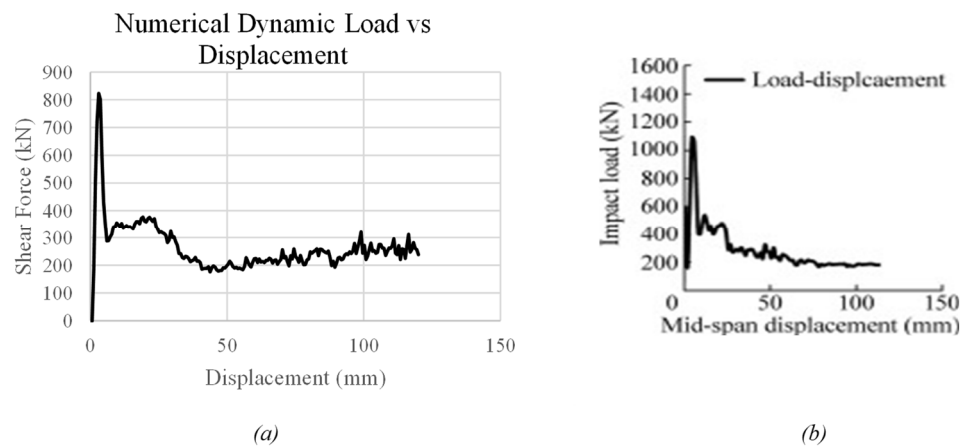


Figure 17. Load vs. displacement (a) calibrated dynamic model and (b) Tahmasebinia et al. [28] dynamic numeric model.

5. Results

Once the model was calibrated within reasonable accuracy, variations of the model were created to test the impact of bolt diameter, steel strength and dynamic loading conditions on the shear performance of dynamic bolts. The following parameters that were tested are listed below in Table 13.

Table 13. Summary of tested variables.

Bolt Diameter (mm)	Steel Yield/Ultimate Stress f_y/f_u (MPa)	Load Sphere Velocity (mm/s)	Load Sphere Mass (kg)
18	550/650	100	33
20	565/685	200	64
23	633/844	400	110
25	847/934	600	175
28	922/1031		
31	1382/1553		

For each conducted test, the assigned history output was used to produce a force vs. time and a displacement vs. time graph with consistent time increments. To obtain a force vs. displacement graph, the ABAQUS combine function was utilised to merge the two outputted graphs. The x and y coordinates of the force vs. displacement graphs were then exported to excel and recorded for analysis.

5.1. Static Results

For static testing, bolt diameter and steel strength were varied to determine the maximum shear force and displacement of the bolt under investigation. A total of 36 static tests were conducted. The effect of varying bolt diameter on maximum shear force and displacement under static loading conditions are compared below in Figure 18. The positive correlation between bolt diameter and ultimate shear strength is consistent across all tested steel yield strengths.

The effect of varying steel yield and ultimate strengths on maximum shear force and displacement under static loading conditions are compared below in Figure 19. The positive correlation between steel strength and ultimate shear strength is apparent across all tested bolt diameters.

5.2. Dynamic Results

For dynamic testing, bolt diameter, steel yield and ultimate strength, load cell velocity and load cell mass were varied to determine the maximum shear force acting on the bolt under investigation, and its respective displacement at failure. Furthermore, the parametric

study also investigated the effect of the above parameters on the energy capacity of the bolt, where the absorbed energy of the system is calculated by integrating the force vs. displacement function [28]. Python, a coding software, was utilised to determine the absorbed energy as a function of displacement. The code is detailed in Appendix A.2. A total of 576 dynamic tests were conducted and recorded.

Static Bolt Diameter Comparison

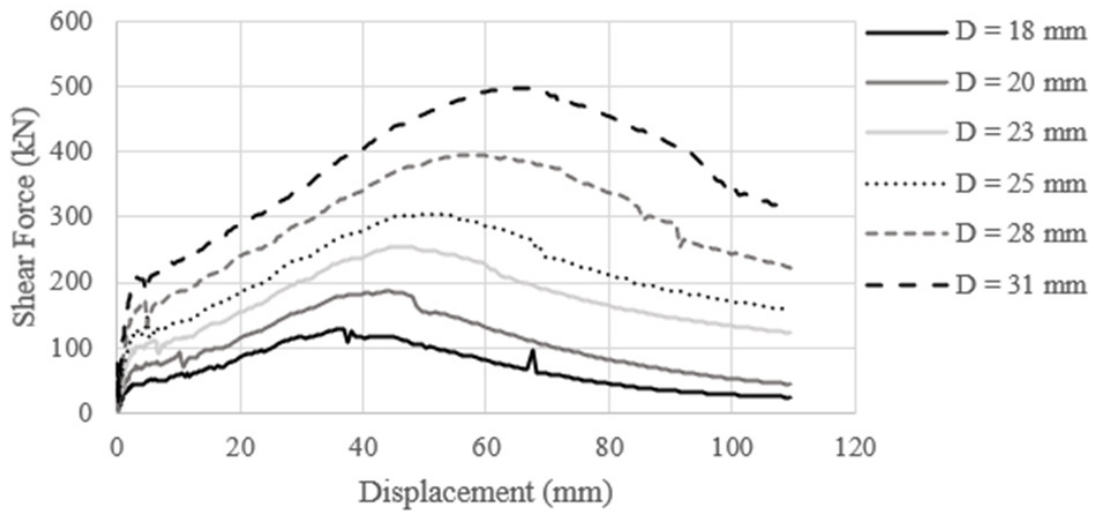


Figure 18. Bolt diameter force vs. displacement comparison for $f_y = 922$ MPa.

Static Steel Strength Comparison

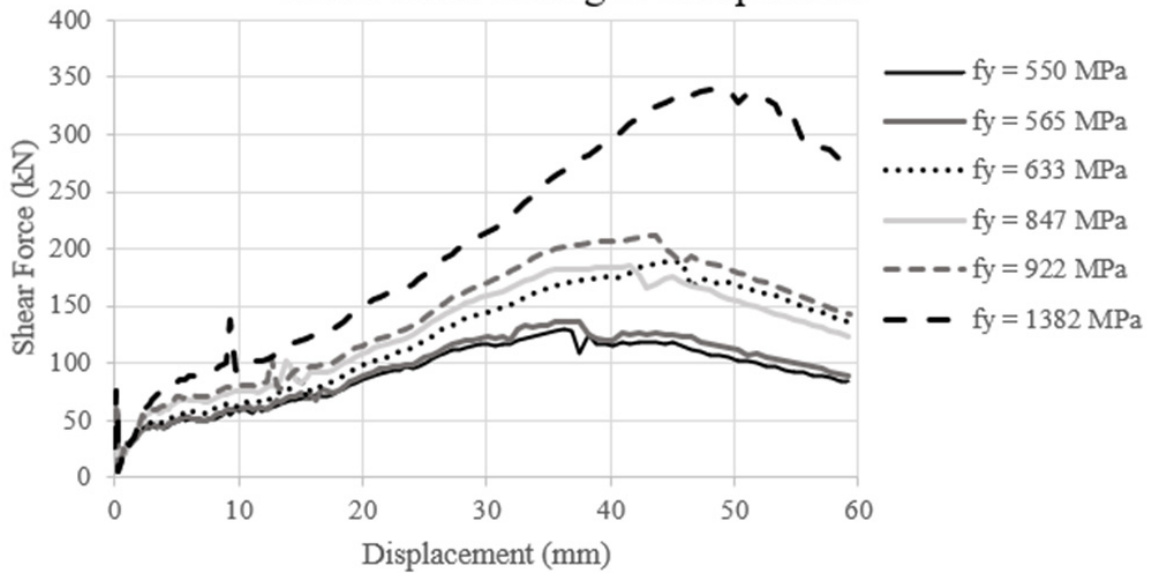
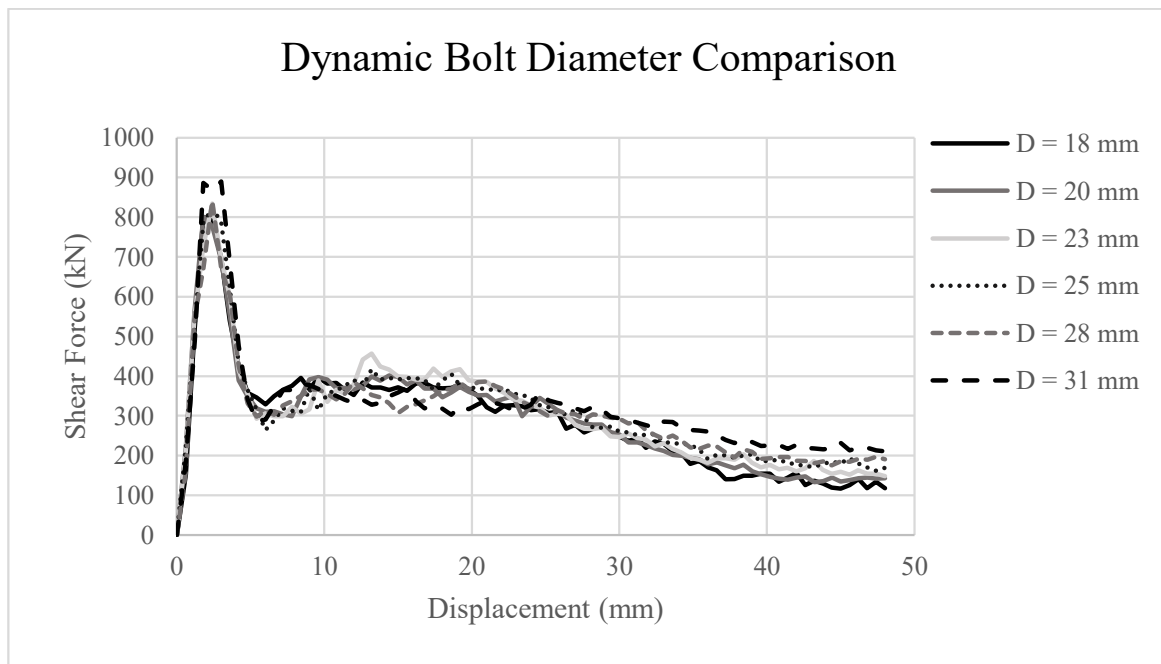
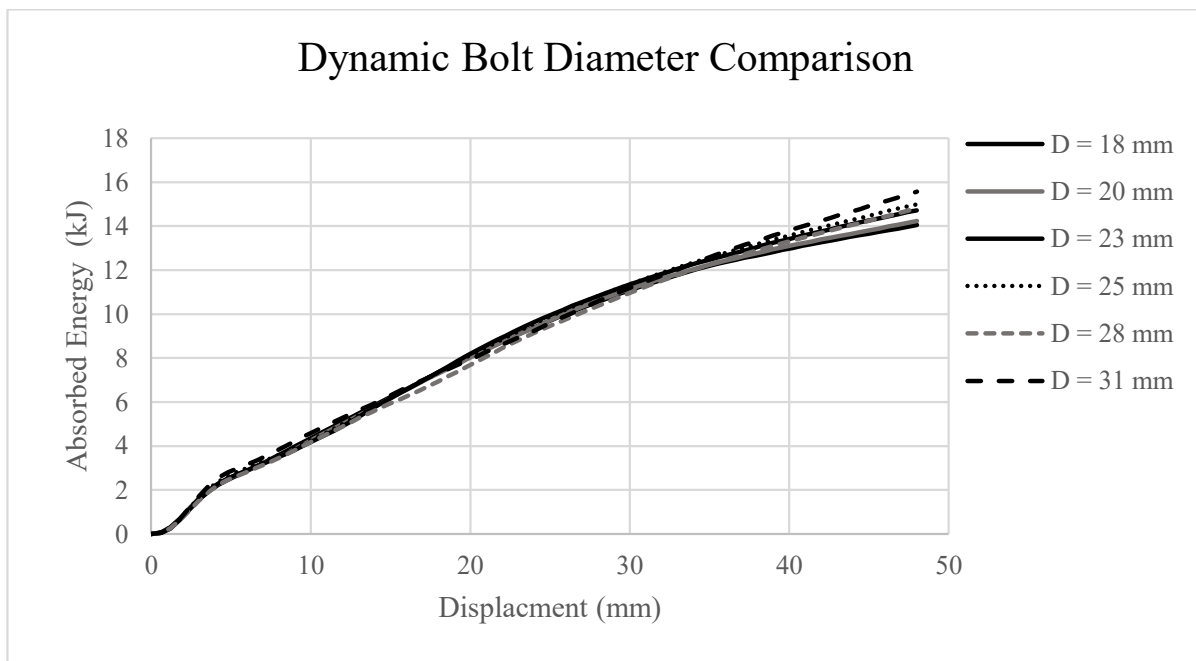


Figure 19. Steel strength force vs. displacement comparison of an 18 mm bolt.

The effect of varying bolt diameters subjected to dynamic loading on a bolt’s energy absorption capacity was examined by considering bolt shear force and displacement. Figure 20 summarises the load vs. displacement and energy absorption vs. displacement graphs of tests 306, 330, 354, 378, 402 and 426, which correspond to a tested steel yield strength of 922 MPa, load cell velocity of 200 mm/s and load cell mass of 110 kg.



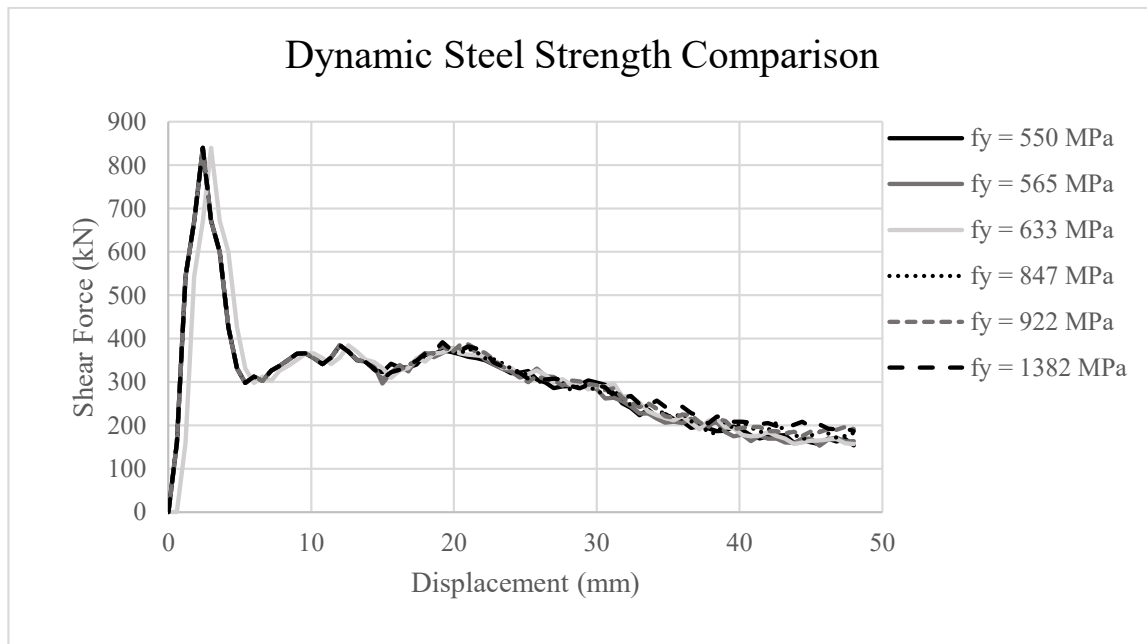
(a)



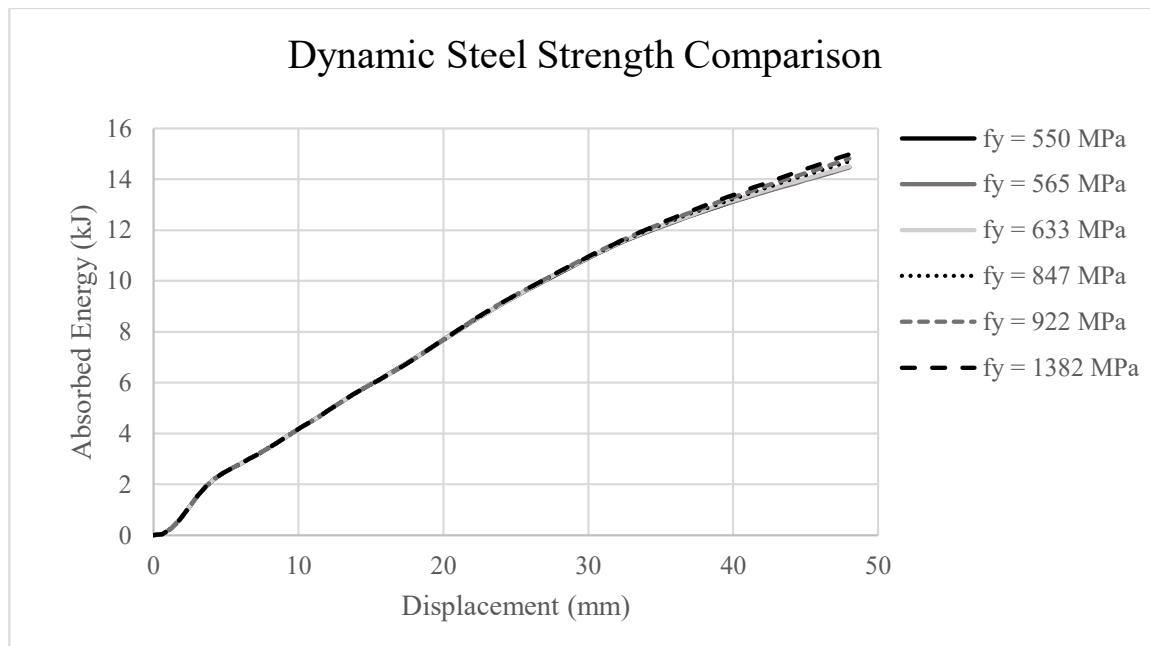
(b)

Figure 20. Bolt diameter comparison of (a) force vs. displacement and (b) absorbed energy vs. displacement.

The effect of varying steel yield and ultimate strength subjected to dynamic loading on a bolt’s energy absorption capacity was examined by considering bolt shear force and displacement. Figure 21 summarises the load vs. displacement and energy absorption vs. displacement graphs of tests 386, 390, 394, 398, 402 and 406 which correspond to a tested bolt diameter of 28 mm, load cell velocity of 200 mm/s and load cell mass of 110 kg.



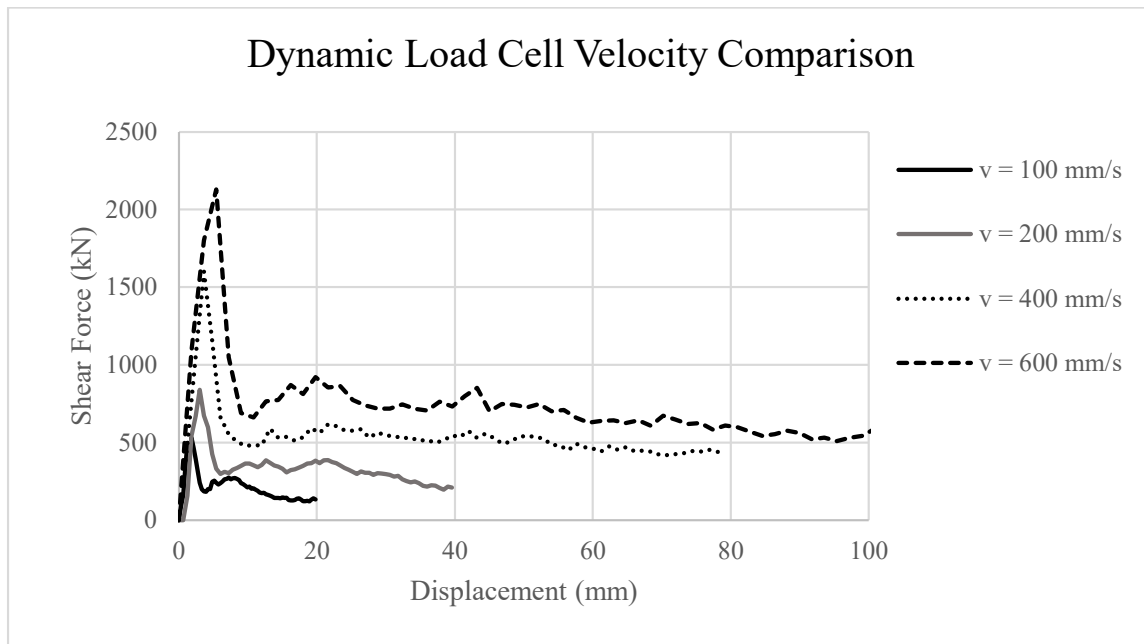
(a)



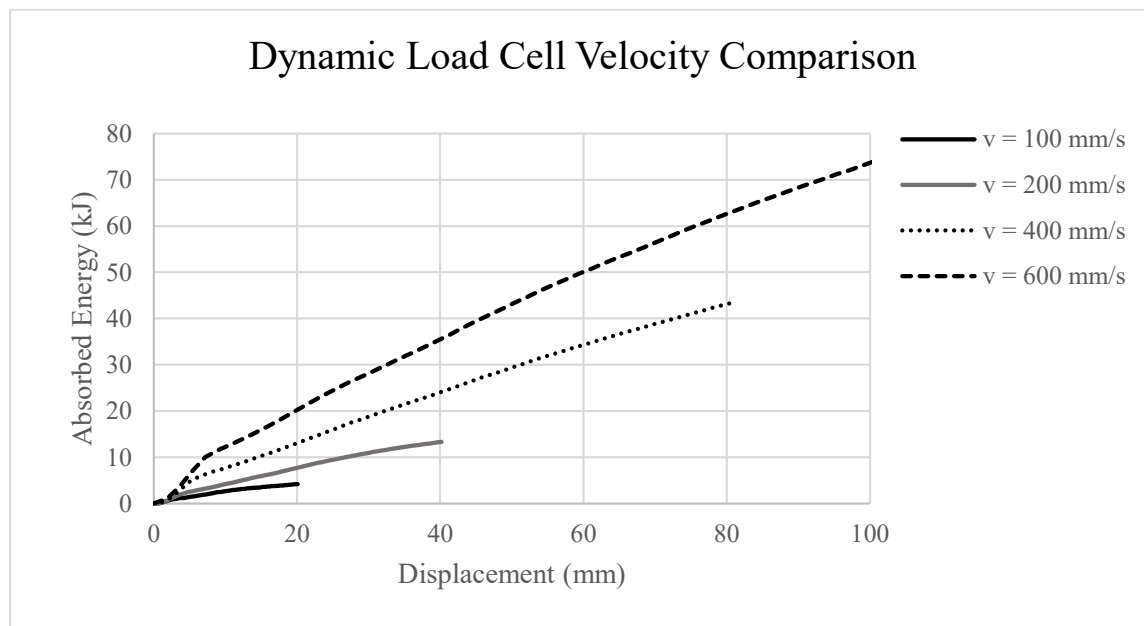
(b)

Figure 21. Steel strength comparison of (a) force vs. displacement and (b) absorbed energy vs. displacement.

The effect of varying the dynamic loading velocity on a bolt’s energy absorption capacity was examined by considering bolt shear force and displacement. Figure 22 summarises the load vs. displacement and energy absorption vs. displacement graphs of tests 401, 402, 403 and 404 which correspond to a tested bolt diameter of 28 mm, steel yield strength of 922 MPa and load cell mass of 110 kg.



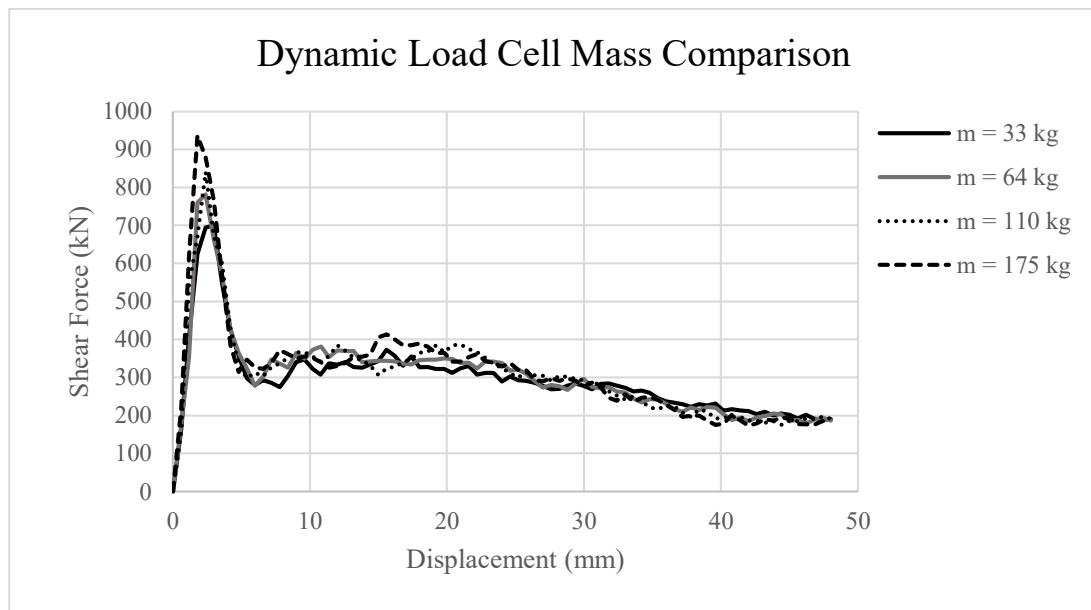
(a)



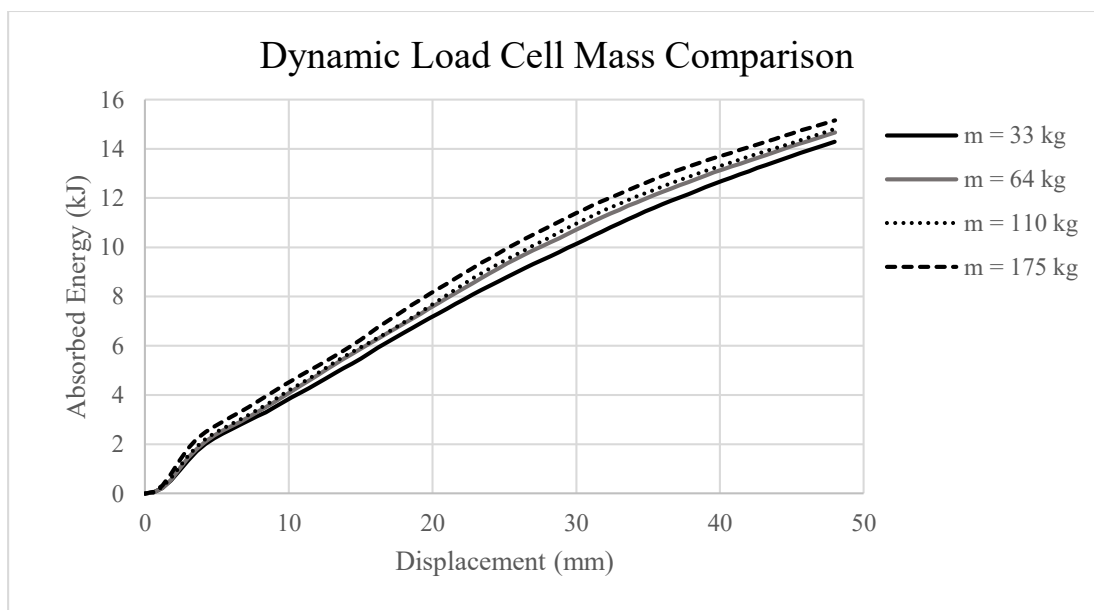
(b)

Figure 22. Load cell velocity comparison of (a) force vs. displacement and (b) absorbed energy vs. displacement.

The effect of varying the dynamic loading mass on a bolt’s energy absorption capacity was examined by considering bolt shear force and displacement. Figure 23 summarises the load vs. displacement and energy absorption vs. displacement graphs of tests 114, 258, 402 and 546, which correspond to a tested bolt diameter of 28 mm, steel yield strength of 922 MPa and load cell velocity of 200 mm/s.



(a)



(b)

Figure 23. Load cell mass comparison of (a) force vs. displacement and (b) absorbed energy vs. displacement.

6. Discussion

6.1. Static Modelling

The static model investigated the impact of varying bolt diameter and steel strengths on the maximum shear load and the respective maximum displacement at ultimate failure. The load vs. displacement graph under static conditions indicates the three distinct stages of shear ductile failure, which include elastic failure, plastic yielding and ultimate failure, as summarised below in Figure 24.

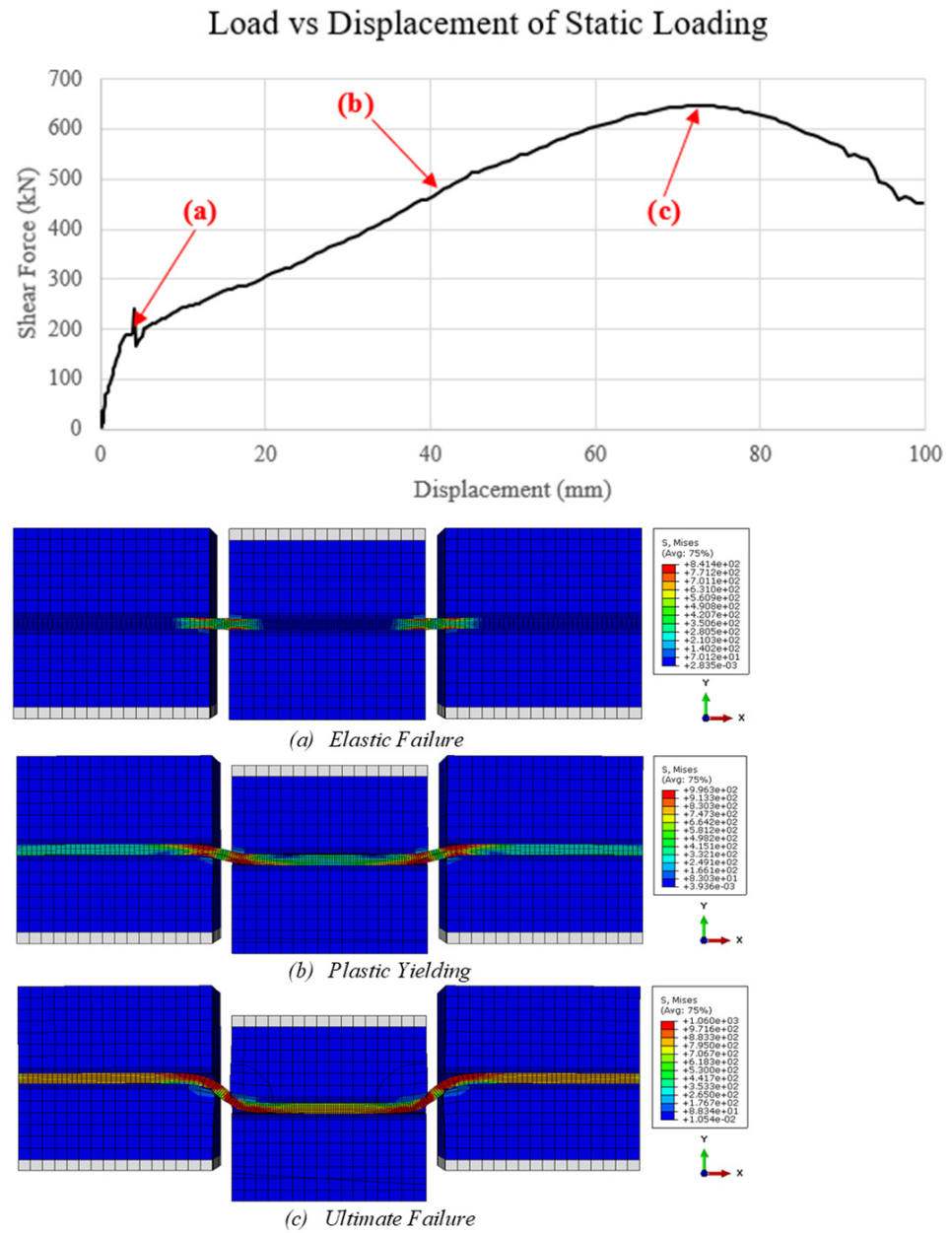


Figure 24. Stages of shear failure under static loading conditions.

The maximum load recorded at ultimate failure has been summarised below in Table 14. As the diameter of the bolt increases, the ultimate shear load at failure increases, which is apparent at all steel strengths. Furthermore, as the steel yield and ultimate strength increases, the maximum shear load increases, which is apparent for all bolt diameters. This was expected as the cross-sectional area and steel yield stress are directly proportional to shear capacity; by increasing either, the maximum shear load will increase. It was observed that for the recorded results of steel yield stress of $f_y = 633$ MPa, similar results were produced for a steel yield stress of $f_y = 847$ MPa. This was most likely due to an input error, and thus should be deemed an outlier for static results.

The maximum displacement at ultimate failure has been summarised below in Table 15. As the diameter of the bolt increases, the ultimate displacement increases, which is apparent at all steel strengths. Furthermore, as the steel yield and ultimate strength increases, the maximum displacement increases, which is apparent for all bolt diameters. The obtained results align with both experimental data and other double shear test numerical simulation [28,29].

Table 14. Maximum shear load of statically loaded bolts.

Bolt Diameter (mm)	Maximum Shear Load (kN)					
	$f_y = 500$ MPa	$f_y = 565$ MPa	$f_y = 633$ MPa	$f_y = 847$ MPa	$f_y = 922$ MPa	$f_y = 1382$ MPa
18	129.0	136.4	189.0	185.0	211.3	339.3
20	186.4	197.5	269.4	270.5	302.0	492.5
23	254.8	272.3	369.2	364.5	409.8	705.7
25	305.1	325.8	443.1	441.3	497.8	848.0
28	394.8	423.0	582.6	575.4	647.0	1084.5
31	498.1	535.5	721.3	716.6	818.4	1301.5

Table 15. Maximum displacement of failure of statically loaded bolts.

Bolt Diameter (mm)	Maximum Displacement at Failure (mm)					
	$f_y = 500$ MPa	$f_y = 565$ MPa	$f_y = 633$ MPa	$f_y = 847$ MPa	$f_y = 922$ MPa	$f_y = 1382$ MPa
18	36.2	36.9	45.1	41.6	43.0	49.5
20	43.6	44.3	51.0	45.1	45.8	60.7
23	45.8	46.5	57.0	51.0	52.5	81.0
25	51.0	53.3	63.8	55.5	60.0	91.5
28	57.8	61.5	76.5	68.2	72.0	109.5
31	65.2	70.5	87.0	76.5	85.5	120.5

6.2. Dynamic Modelling

The dynamic model simulated impact loading, where a sphere of known mass and velocity was dropped onto the centre block of the double shear test. The load sphere transfers the energy from the load cell into the concrete block which is then transmitted to the bolt under investigation. To reflect experimental impact load tests, the field and history output was assigned to the load sphere, where the recorded load was reflective of the reaction forces experienced by the rigid loading cell. Similarly, the recorded displacement was a measure of the mid span deflection of the load sphere. Therefore, the displacement at failure cannot be determined, and thus, maximum deflection is considered at the ultimate strength. The load-displacement graph displays an initial inertial spike, which reduces because of damping [5]. The kinetic energy transferred from the bolt to the concrete box is then transferred to the bolt, causing it to deform and fail in a combination of shear and tension. The second peak of the load displacement graph will be considered as the bolt's ultimate load, which is represented below in Figure 25.

The impact of bolt diameter, steel yield and ultimate strength, load cell velocity and load cell mass on the bolt's maximum load, displacement and absorbed energy will be further discussed below.

6.2.1. Bolt Diameter

As the load cell is dropped onto the concrete box, momentum is transferred from the load sphere to the bolt through the concrete encasing. As diameter of the bolt increases, there is no apparent increase of displacement. As the testing environment is a closed system, momentum and thus kinetic energy absorbed by the system should not change, which is reflected by the initial trend of the absorbed energy vs. displacement graph of the varying bolt diameters. However, as the bolt diameter influences the maximum shear displacement of the bolt, as the bolt diameter increases, the longer the bolt takes to reach failure, resulting in the bolt working longer and thus absorbing more energy. This is represented in the later stage of the absorbed energy vs. displacement graph, where bolts with larger diameters shows slightly more absorbed energy.

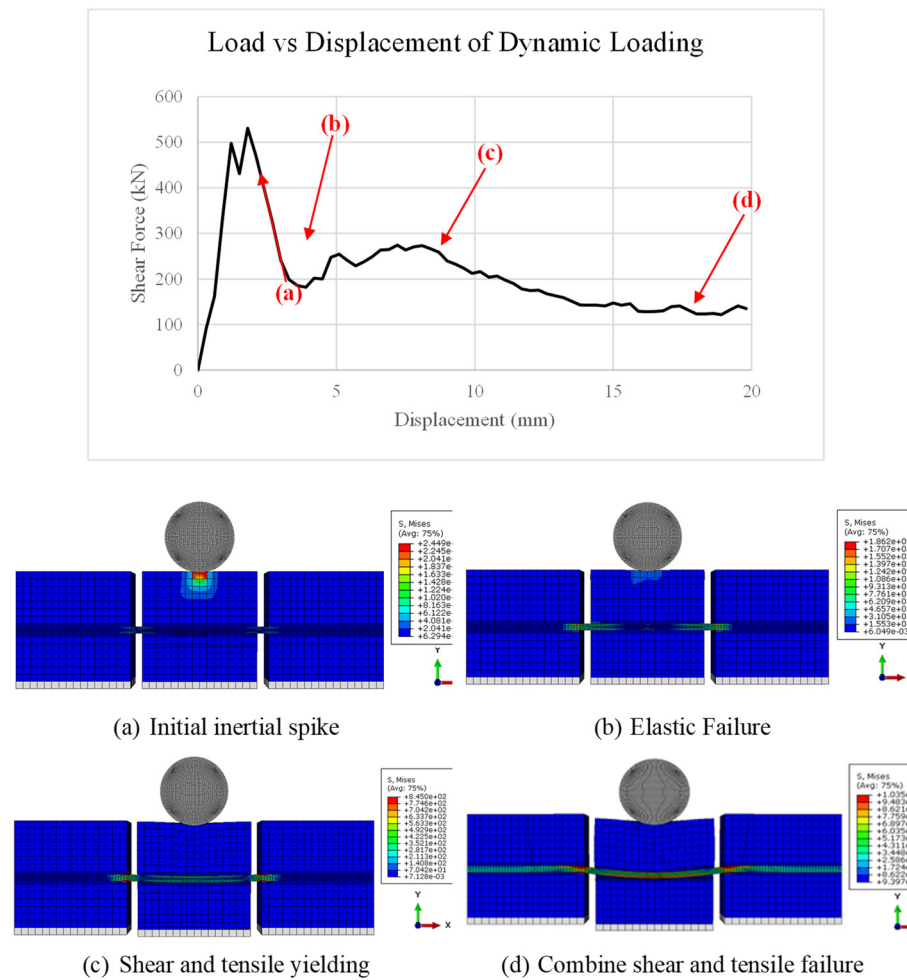


Figure 25. Failure of dynamically loaded bolt.

6.2.2. Steel Yield and Ultimate Strength

As the steel yield and ultimate strength of the steel increases, the force vs. displacement graph displays an identical trend for varying steel yield and ultimate stresses. Similar to bolt diameter, as steel strength increases, the maximum resistive force and displacement of the bolt does not change, however, the time taken for the bolt to reach yield stress and ultimately fail increases. As a result, as steel strength increases, the longer the tested bolt resists forces till failure, thus working longer and absorbing more energy.

6.2.3. Load Cell Velocity

As the load cell velocity is increased, the initial inertial force recorded in the load vs. displacement graphs increases. This was expected as the greater the velocity of the load sphere, the greater the amount of kinetic energy transferred from the moving load sphere to the stationary concrete encasing, as kinetic energy is directly proportional to the square of velocity. The equation below represents the relationship between kinetic energy, mass and velocity.

$$E_k = \frac{1}{2}mv^2$$

Furthermore, the greater the velocity of the load cell, the greater the resisted shear force of the bolt and its respective displacement at the bolt’s ultimate stress. This occurs as the bolt must resist a greater force, due to an increased input.

As the load cell velocity increases, the absorbed energy also increases. This is expected as kinetic energy is proportional to the square of velocity applied, thus, if the velocity is doubled, the absorbed energy is theoretically quadrupled. For the 28 mm diameter bolt,

with an applied load cell velocity of 200 mm/s, 13.3 kJ of energy is absorbed, whilst at a load cell velocity of 400 mm/s, 43.3 kJ of energy is absorbed.

$$\frac{\text{Absorbed Energy}_{v=400 \text{ mm/s}}}{\text{Absorbed Energy}_{v=200 \text{ mm/s}}} = \frac{43.3 \text{ kJ}}{13.3 \text{ kJ}} = 3.26$$

The results show that by doubling the velocity of the load cell, the absorbed energy is marginally less than the expected quadrupled value. This was identified due to material damping, which causes a fraction of the energy to dissipate rather than being transferred as kinetic energy upon impact loading

6.2.4. Load Cell Mass

As the load sphere diameter is increased, as the density is kept constant, the mass of the load cell is increased. As the mass of the load cell increases, the initial inertial force recorded in the load vs. displacement graphs increases. This was expected as the greater the mass of the load sphere, the greater the amount of kinetic energy transferred from the moving load sphere to the stationary concrete encasing, as mass is directly proportional to the kinetic energy. Furthermore, the greater the mass of the load cell, the greater the resisted shear force of the bolt and its respective displacement at the bolt's ultimate stress. As the mass of the load sphere increases, the absorbed energy of the system increases, which was expected as kinetic energy is directly proportional to mass.

6.3. Static vs. Dynamic Comparison

When designing a rock bolt suitable for rock-burst prone conditions, both static and dynamic loading conditions need to be considered. Figure 26 compares the statically and dynamically loaded force vs. displacement graph of the tested bolt with a diameter of 28 mm and steel yield strength of 922 MPa.

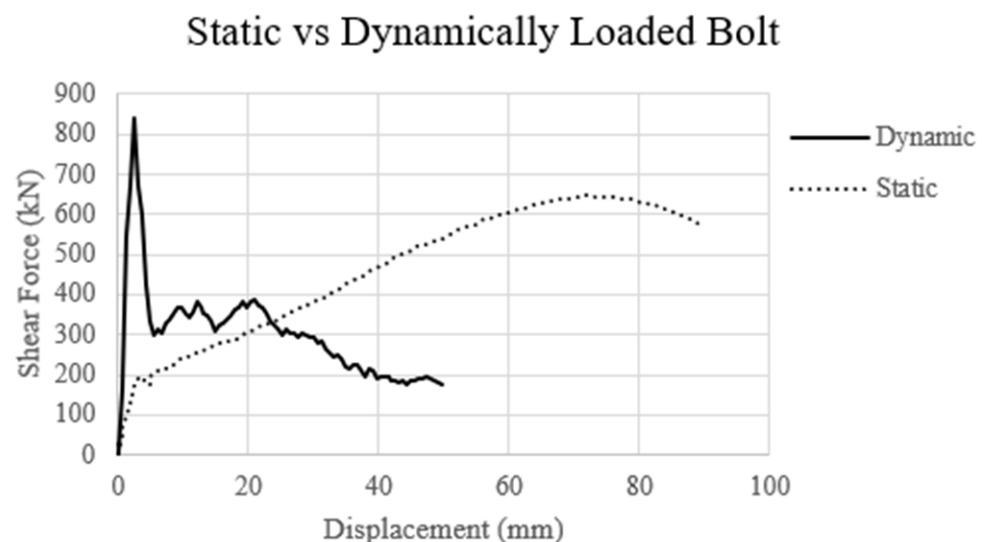


Figure 26. Static vs. dynamic load vs. displacement comparison.

By comparing the static and dynamic load vs. displacement results, the failure mechanisms and the effected bolt capacity can be identified. Under static loading conditions, the bolt undergoes failure at the later stage of loading, where the bolt fails as load increases. Under dynamic loading conditions, the bolt fails in the initial loading stage, due to the impact of higher strain rates. Thus, in dynamically loaded conditions, such as rock burst prone excavations, the dynamic capacity of the bolt is critical.

7. Limitations of the Study

7.1. Model Simplification

Two major simplifications were made when creating the numerical model, which included simplifying the geometric features of the tested cable and rock bolts and omitting bolt grouting. For this parametric study, all bolts were modelled as smooth cylinders, which does not represent the true nature of bolts. Geometric properties omitted include general cross-sectional shapes, indented wires, angle of twist, bulbed strands, anchors and threaded sections.

Furthermore, when creating the model, the diameter of the hole created in the concrete box was equal to the diameter of the bolt under investigation, where grouting of the bolt was replaced using surface-to-surface contact properties. When installing a bolt in the field, the bored hole is greater than the diameter of the bolt. The bolt is anchored into the excavation face by grouting with a resin or cementitious grout. Thus, this model excludes the bolt-grout and grout-rock interactions that occur in the field.

7.2. Numerical Model Calibration

To calibrate the static model at an accuracy of approximately 80%, many iterations of the ABAQUS model were created. Although The simplifications are deemed to be reasonable, the numerical model did not completely replicate the experimental test used. The model developed was designed with a 50 mm gap between each concrete block such that there no would be no friction between the concrete blocks. This was done to avoid an excess amount of contact regions, as the greater the amount of contact points, the more likely the model is to experience convergence issues and the greater will be the computational time.

The experimental test does not incorporate such means, thus the applied load recorded in the experimental data is inclusive of the forces required to overcome the friction created by the contact between concrete blocks. Aziz et al. (2015) [37] mathematical estimation, using the Mohr–Coulomb and Fourier series relationship, has been utilised to estimate that approximately 30% of the recorded shear load applied was used to overcome the friction forces created by the contact of the concrete boxes. Thus, the numerical model underestimating the shear load of the bolt is expected.

7.3. Mesh Accuracy

The dynamic test used a coarse mesh for the concrete box, which reduced the accuracy of the results as energy was transferred to from the load sphere to the bolt through the concrete. By incorporating a finer mesh, more accurate results can be produced. Figure 27 shows a concrete box that incorporates finer mesh and compares it to the mesh used in the study.

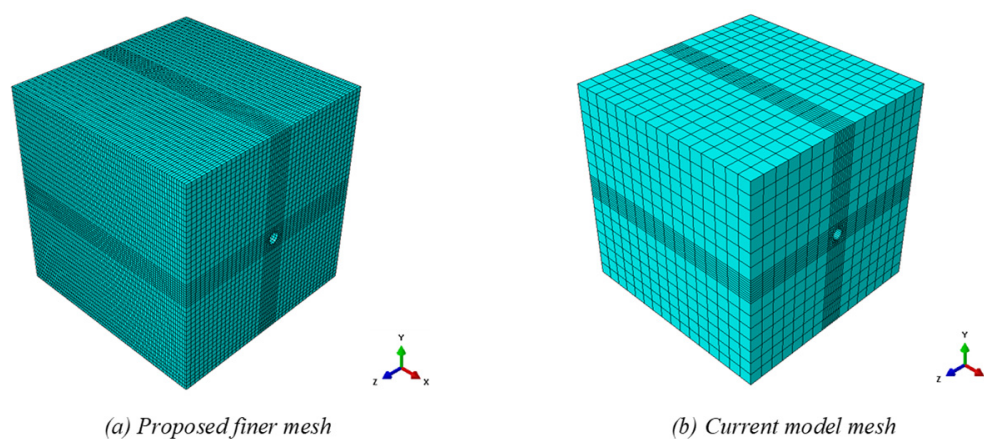


Figure 27. Comparison of proposed concrete box mesh with current mesh.

Dynamic testing with the parameters of a 28 mm bolt diameter, 922 MPa steel yield strength, 200 mm/s load cell velocity and 110 kg load cell mass was carried out to compare the results of two meshes. The load vs. displacement of both meshes are shown below in Figure 28. The finer concrete mesh produces a load vs. displacement graph with less fluctuations and a more definable ultimate stress of 379.6 kN. On the other hand, the coarser concrete mesh produces multiple fluctuations, which creates difficulties determining the ultimate stress of the bolt. However, although the finer mesh is more accurate, the computational time of the finer mesh increased by 1229%, which is not feasible to run many tests.

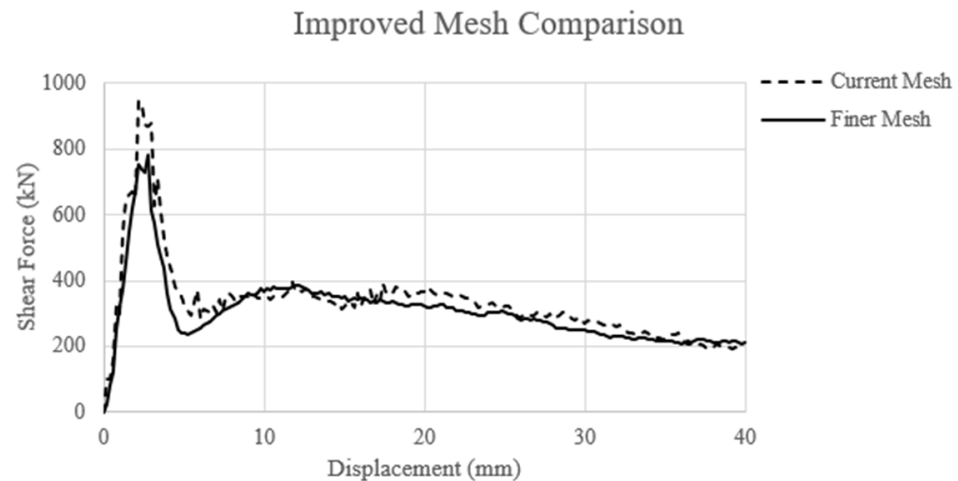


Figure 28. Load vs. displacement comparison of current concrete mesh and proposed finer mesh.

8. Conclusions

A finite element model of a double shear test was successfully developed in ABAQUS/Explicit to assess the impact of various parameters on cable bolt capacity. The statically loaded model was initially calibrated and validated against experimental data at an accuracy of 80%. The dynamically loaded model was successfully constructed as an extension of the static model and was consistent with the existing literature.

The parametric study investigated the influence of bolt diameter, steel yield and ultimate strength, dynamic load mass and dynamic load velocity against the shear and deformation capacity of cable bolts. This was furthered to determine the influence of such parameters on the energy absorption capacity of cable bolts subjected to dynamic loads. The results indicate a positive correlation between bolt capacity subject to dynamic loading and bolt diameter, steel strength, load velocity and mass. Whilst the study produces valuable data in furthering the understanding of cable bolts in dynamic conditions, the results can be furthered by addressing the limitations of numerical model simplifications, calibration accuracy and meshing. Overall, a novel Finite Element Model was developed to predict actual capacity of cable bolts due to changing different geometrical and material properties. The suggested model is a cost-effective solution for future technical investigations.

Future Work

The dynamic model can be further improved to produce more accurate results. It is recommended that the model is recalibrated against experimental data of a double shear test that incorporates frictionless shearing between concrete blocks. This will increase the accuracy of the numerical model's calibration. In addition to recalibrating the model, the model can be further improved by increasing the fineness of the concrete mesh.

Furthermore, more parameters that impact cable bolt energy absorption and shear capacity can be investigated, such as effective cable length, bolt geometry, angle of bolt insertion and pretension loads. Regression analysis can also further the significance of the

results obtained and thus should be utilised to determine the relationship of bolt diameter, steel strength, loading velocity and mass on the dynamic capacity of cable bolts.

Author Contributions: Conceptualization: F.T., A.Y. and P.F.; methodology: F.T., A.Y. and P.F.; software: F.T., A.Y. and P.F.; Validation: F.T., A.Y. and P.F.; formal analysis: F.T., A.Y. and P.F.; investigation: F.T., A.Y. and P.F. resources: F.T. and K.S.; data curation: F.T., A.Y. and P.F.; writing—original draft preparation: F.T., A.Y. and P.F.; writing—review and editing, F.T.; visualization: F.T., A.Y., P.F. and K.S.; Supervision, F.T. and K.S.; project administration: F.T. and K.S.; funding acquisition: F.T. and K.S. All authors have read and agreed to the published version of the manuscript.

Funding: This research received no external funding.

Institutional Review Board Statement: Not applicable.

Informed Consent Statement: Not applicable.

Data Availability Statement: Not applicable.

Conflicts of Interest: The authors declare no conflict of interest.

Appendix A

Appendix A.1

Python code to estimate fracture energy of steel.

```

from google.colab import drive
drive.mount('/content/gdrive')

import numpy as np
import pandas as pd
import matplotlib.pyplot as plt
import csv

dataset_path = "gdrive/My Drive/Colab Notebooks/thesis/stressstrain.csv"
import csv

with open(dataset_path, newline = "") as csvfile:
    data = list(csv.reader(csvfile, delimiter = '\n'))
new_array = []
for thing in data:
    for string in thing:
        string = string.split(",")
        for element in string:
            element.strip(",")
            string[:] = [x for x in string if x]
            new_array.append(string)
new_array = [x for x in new_array if x]
newer_array = []
for line in new_array:
    if len(line) == 144:
        line = [val for val in line for _ in (0, 1)]
        newer_array.append(line)
    else:
        try:
            line = [float(x) for x in line]
            newer_array.append(line)
        except ValueError:
            continue
coords_with_names = newer_array

```

```

list_t_names = np.array(coords_with_names).T.tolist()
coords = newer_array[1:]
list_t = np.array(coords).T.tolist()

from scipy import integrate

table = []
i = 0

while True:
    if i > 286:
        break

    table_row = []
    table_sums = []

    x = list_t[i]
    y = list_t[i + 1]
    y_int = integrate.cumtrapz(y, x, initial = 0)
    y_int_sum = np.trapz(y, x)

    name = list_t_names[i]
    table_row.append(name[0])
    for integral in y_int:
        table_row.append(integral)

    table.append(table_row)
    table_sums.append(y_int_sum)

    plt.plot(x, y_int, 'r', label = 'test 1')
    plt.legend(loc = 'best')
    plt.show
    i += 2

np_table = np.array(table).T.tolist()

file = open('gdrive/My Drive/Colab Notebooks/thesis/fractureresults.csv', 'w')
writer = csv.writer(file)

for row in np_table:
    writer.writerow(row)

file.close()

```

Appendix A.2

Python code to calculate absorbed energy as a function of measured displacement.

```

from google.colab import drive
drive.mount('/content/gdrive')

import numpy as np
import pandas as pd
import matplotlib.pyplot as plt
import csv

dataset_path = "gdrive/My Drive/Colab Notebooks/thesis/dynamicdata.csv"
import csv

with open(dataset_path, newline = "") as csvfile:
    data = list(csv.reader(csvfile, delimiter = '\n'))

new_array = []

for thing in data:
    for string in thing:

```

```
string = string.split(",")
for element in string:
    element.strip(",")
    string[:] = [x for x in string if x]
    new_array.append(string)
new_array = [x for x in new_array if x]
newer_array = []
for line in new_array:
    if len(line) == 144:
        line = [val for val in line for _ in (0, 1)]
        newer_array.append(line)
    else:
        try:
            line = [float(x) for x in line]
            newer_array.append(line)
        except ValueError:
            continue
coords_with_names = newer_array
list_t_names = np.array(coords_with_names).T.tolist()
coords = newer_array[1:]
list_t = np.array(coords).T.tolist()
from scipy import integrate
table = []
i = 0
while True:
    if i > 286:
        break
    table_row = []
    x = list_t[i]
    y = list_t[i + 1]
    y_int = integrate.cumtrapz(y, x, initial = 0)
    name = list_t_names[i]
    table_row.append(name[0])
    for integral in y_int:
        table_row.append(integral)
    table.append(table_row)
    plt.plot(x, y_int, 'r', label = 'test 1')
    plt.legend(loc = 'best')
    plt.show
    i += 2
np_table = np.array(table).T.tolist()
file = open('gdrive/My Drive/Colab Notebooks/thesis/energyresults.csv', 'w')
writer = csv.writer(file)
for row in np_table:
    writer.writerow(row)
file.close()
```

References

1. Feng, X.-T.; Xiao, Y.-X.; Feng, G.-L.; Yao, Z.; Chen, B.; Yang, C.; Su, G. Study on the development process of rockbursts. *Chin. J. Rock Mech. Eng.* **2019**, *38*, 649–673.
2. Potvin, Y.; Wesseloo, J. Towards an understanding of dynamic demand on ground support. *J. South. Afr. Inst. Min. Metall.* **2013**, *113*, 913–922. Available online: http://www.scielo.org.za/scielo.php?script=sci_arttext&pid=S2225-62532013001200007&nrm=iso (accessed on 17 November 2022).
3. Durrheim, R.J.; Milev, A.M.; Spottiswoode, S.M.; Vakalisa, B. Improvement of worker safety through the investigation of the site response to rockbursts. *CSIR 1997*. Available online: <http://hdl.handle.net/10204/1690> (accessed on 17 November 2022).
4. Zhang, C.; Canbulat, I.; Hebblewhite, B.; Ward, C.R. Assessing coal burst phenomena in mining and insights into directions for future research. *Int. J. Coal Geol.* **2017**, *179*, 28–44. [[CrossRef](#)]
5. Tahmasebinia, F.; Zhang, C.; Wei, C.; Canbulat, I.; Saydam, S.; Sepasgozar, S. A new concept to design combined support under dynamic loading using numerical modelling. *Tunn. Undergr. Space Technol.* **2021**, *117*, 104132. [[CrossRef](#)]
6. Hadjigeorgiou, J.; Potvin, Y. A Critical Assessment of Dynamic Rock Reinforcement and Support Testing Facilities. *Rock Mech. Rock Eng.* **2011**, *44*, 565–578. [[CrossRef](#)]
7. Potvin, Y.; Wesseloo, J.; Heal, D. An interpretation of ground support capacity submitted to dynamic loading. *Trans. Inst. Min. Metall. Sect. A Min. Technol.* **2010**, *119*, 233–245. [[CrossRef](#)]
8. Stacey, T.R. A philosophical view on the testing of rock support for rockburst conditions. *J. South Afr. Inst. Min. Metall.* **2012**, *112*, 1–8. Available online: http://www.scielo.org.za/scielo.php?script=sci_arttext&pid=S2225-62532012000800007&nrm=iso (accessed on 17 November 2022).
9. He, M.; Ren, F.; Liu, D. Rockburst mechanism research and its control. *Int. J. Min. Sci. Technol.* **2018**, *28*, 829–837. [[CrossRef](#)]
10. Roberts, T.; Talu, S.; Wang, Y. Design and Testing of High Capacity Surface Support. 2018. Available online: <https://www.ausimm.com/publications/conference-proceedings/the-fourth-australasian-ground-control-in-mining-conference-ausrock/design-and-testing-of-high-capacity-surface-support/> (accessed on 17 November 2022).
11. Brown, E. *Underground Excavations in Rock*; CRC Press: Boca Raton, FL, USA, 1980.
12. Hildyard, M.W.; Milev, A. Simulated rockburst experiment: Development of a numerical model for seismic wave propagation from the blast, and forward analysis. *J. South Afr. Inst. Min. Metall.* **2001**, *101*, 235–245.
13. Li, X.; Gong, F.; Tao, M.; Dong, L.; Du, K.; Ma, C.; Yin, T. Failure mechanism and coupled static-dynamic loading theory in deep hard rock mining: A review. *J. Rock Mech. Geotech. Eng.* **2017**, *9*, 767–782. [[CrossRef](#)]
14. Heal, D.; Hudyma, M.; Potvin, Y. Assessing the in-situ performance of ground support systems subjected to dynamic loading. In Proceedings of the Ground Support in Mining and Underground Construction, Proceedings of the Fifth International Symposium on Ground Support, Perth, Australia, 28 September 2004.
15. Hagan, D.M.; Milev, T.O.; Spottiswoode, A.M.; Hildyard, S.M.; Grodner, M.W.; Rorke, M.; Le Bron, A.T. Simulated rockburst experiment—An overview. *J. South Afr. Inst. Min. Metall.* **2001**, *101*, 217–222. [[CrossRef](#)]
16. Kaiser, P.K.; Cai, M. Design of rock support system under rockburst condition. *J. Rock Mech. Geotech. Eng.* **2012**, *4*, 215–227. [[CrossRef](#)]
17. Archibald, J.F.; Baidoes, J.P.; Katsabanis, P.T. Comparative assessment of conventional support systems and spray-on rock linings in a rockburst prone environment. In Proceedings of the 3rd International Seminar on Surface Support Liners: Thin Spray-on Liners, Shotcrete and Mesh, Quebec City, QC, Canada, 25–27 August 2003.
18. Jing, L.; Hudson, J.A. Numerical methods in rock mechanics. *Int. J. Rock Mech. Min. Sci.* **2002**, *39*, 409–427. [[CrossRef](#)]
19. Miranda, E.E. Deformation and Fracture of Concrete under Uniaxial Impact Loading. Ph.D. Thesis, University of Missouri, Columbia, MO, USA, 1972.
20. Blake, W. Rock-burst mechanics. *Q. Colo. Sch. Mines* **1972**, *67*, 1–64. Available online: <https://www.osti.gov/biblio/5298057> (accessed on 17 November 2022).
21. Ortlepp, W.D. The behaviour of tunnels at great depth under large static and dynamic pressures. *Tunn. Undergr. Space Technol.* **2001**, *16*, 41–48. [[CrossRef](#)]
22. Ortlepp, W.D.; Stacey, T.R. Rockburst mechanisms in tunnels and shafts. *Tunn. Undergr. Space Technol.* **1994**, *9*, 59–65. [[CrossRef](#)]
23. Jing, L. A review of techniques, advances and outstanding issues in numerical modelling for rock mechanics and rock engineering. *Int. J. Rock Mech. Min. Sci.* **2003**, *40*, 283–353. [[CrossRef](#)]
24. Castro, L.M.; Bewick, R.; Carter, T. An overview of numerical modelling applied to deep mining. In *Innovative Numerical Modeling in Geomechanics*; CRC Press: Boca Raton, FL, USA, 2012; pp. 393–414. [[CrossRef](#)]
25. Vlachopoulos, N.; Diederichs, M.S. Appropriate Uses and Practical Limitations of 2D Numerical Analysis of Tunnels and Tunnel Support Response. *Geotech. Geol. Eng.* **2014**, *32*, 469–488. [[CrossRef](#)]
26. Zivaljic, N.; Smoljanovic, H.; Nikolic, Z. A combined finite-discrete element model for RC structures under dynamic loading. *Eng. Comput.* **2013**, *30*, 982–1010. [[CrossRef](#)]
27. Wang, J.; Apel, D.B.; Pu, Y.; Hall, R.; Wei, C.; Sepehri, M. Numerical modeling for rockbursts: A state-of-the-art review. *J. Rock Mech. Geotech. Eng.* **2021**, *13*, 457–478. [[CrossRef](#)]
28. Tahmasebinia, F.; Zhang, C.; Canbulat, I.; Vardar, O.; Saydam, S. Numerical and analytical simulation of the structural behaviour of fully grouted cable bolts under impulsive loading. *Int. J. Min. Sci. Technol.* **2018**, *28*, 807–811. [[CrossRef](#)]

29. Mirzaghobanali, A.; Rasekh, H.; Aziz, N.; Yang, G.; Khaleghparast, S.; Nemcik, J. Shear strength properties of cable bolts using a new double shear instrument, experimental study, and numerical simulation. *Tunn. Undergr. Space Technol.* **2017**, *70*, 240–253. [[CrossRef](#)]
30. Bahaaddini, M.; Hagan, P.C.; Mitra, R.; Hebblewhite, B.K. Scale effect on the shear behaviour of rock joints based on a numerical study. *Eng. Geol.* **2014**, *181*, 212–223. [[CrossRef](#)]
31. Zafar, A.; Andrawes, B. Incremental dynamic analysis of concrete moment resisting frames reinforced with shape memory composite bars. *Smart Mater. Struct.* **2012**, *21*, 025013. [[CrossRef](#)]
32. Arasaratnam, P.; Sivakumaran, K.S.; Tait, M.J. True Stress-True Strain Models for Structural Steel Elements. *ISRN Civ. Eng.* **2011**, *2011*, 656401. [[CrossRef](#)]
33. Ardalan, M.; Deam, B.; Fragiaco, M. Experimental results of fracture energy and fracture toughness of Radiata Pine laminated veneer lumber (LVL) in mode I (opening). *Mater. Struct.* **2012**, *45*, 1189–1205. [[CrossRef](#)]
34. Hajikarimi, P.; Moghadas Nejad, F. Chapter 7-Application of viscoelasticity for experimental tests. In *Applications of Viscoelasticity*; Hajikarimi, P., Nejad, F.M., Eds.; Elsevier: Amsterdam, The Netherlands, 2021; pp. 141–180.
35. Sumer, Y.; Aktas, M. Defining parameters for concrete damage plasticity model. *Chall. J. Struct. Mech.* **2015**, *1*, 149–155. [[CrossRef](#)]
36. ABAQUSinc. ABAQUS Analysis User's Manuals. 2009. Available online: <http://130.149.89.49:2080/v6.14/books/usb/default.htm> (accessed on 17 November 2022).
37. Aziz, N.; Craig, P.; Mirzaghobanali, A.; Rasekh, H.; Nemcik, J.; Li, X. *Behaviour of Cable Bolts in Shear; Experimental Study and Mathematical Modelling*; University of Wollongong: Wollongong, NSW, Australia, 2015.
38. Krykovskiy, O.; Krykovska, V.; Skipochka, S. Interaction of rock-bolt supports while weak rock reinforcing by means of injection rock bolts. *Min. Miner. Depos.* **2021**, *15*, 8–14. [[CrossRef](#)]

Disclaimer/Publisher's Note: The statements, opinions and data contained in all publications are solely those of the individual author(s) and contributor(s) and not of MDPI and/or the editor(s). MDPI and/or the editor(s) disclaim responsibility for any injury to people or property resulting from any ideas, methods, instructions or products referred to in the content.